A semi-implicit fractional step method immersed boundary method for the numerical simulation of natural convection non-Boussinesq flows

Dmitry Zviaga[1], Ido Silverman[2], Alexander Gelfgat[3] and Yuri Feldman[1]

[1] Department of Mechanical Engineering, Ben-Gurion University of the Negev, P.O. Box 653, Beer-Sheva 84105, Israel.
[2] Soreq Nuclear Research Center, 81000 Yavne, Israel.
[3] School of Mechanical Engineering, Tel Aviv University, Tel Aviv 6997801, Israel.

Abstract. The paper presents a novel pressure-corrected formulation of the immersed boundary method (IBM) for the simulation of fully compressible non-Boussinesq natural convection flows. The formulation incorporated into the pressure-based fractional step approach facilitates simulation of the flows in the presence of an immersed body characterized by a complex geometry. Here, we first present extensive grid independence and verification studies addressing incompressible pressure-driven flow in an extended channel and non-Boussinesq natural convection flow in a differentially heated cavity. Next, the steady-state non-Boussinesq natural convection flow developing in the presence of hot cylinders of various diameters placed within a cold square cavity is thoroughly investigated. The obtained results are presented and analyzed in terms of the spatial distribution of path lines and temperature fields and of heat flux values typical of the hot cylinder and the cold cavity surfaces. Flow characteristics of multiple steady-state solutions discovered for several configurations are presented and discussed in detail.

Key words: natural convection non-Boussinesq flows, pressure-corrected immersed boundary method, multiple steady state solutions.

1 Introduction

The ability to accurately simulate natural convection flows is critical for a wide range of engineering applications, including cooling electronic equipment, minimizing heat losses in buildings, investigating atmospheric flows, modeling heat transfer, and preventing accidents in the nuclear industry, to name but a few. The methods typically utilized for the simulation of natural convection flows can be classified into two major groups, one relying on weakly compressible approximations and the other addressing the fully compressible flow, as extensively reviewed in [1]. The first group of methods treats the flow

as incompressible. In these methods, the buoyancy is introduced by employing either the Boussinesq approximation, which accounts for density variations in the gravity term and may also account for variations in the thermophysical properties of the flow, or Gay-Lussac-type approximations, which account for density variations in both the gravity and advection terms. The second group uses fully compressible Navier Stokes (NS) and energy equations.

The majority of weakly compressible approximations, which were developed for the simulation of low-Mach-number compressible flows, are based on an asymptotic model. The asymptotic model for the simulation of thermally driven natural convection flows was formulated for the first time in [2] and is known in the literature as the "classical low-Mach-number model." The key idea was to split the pressure field into a large, time-dependent thermodynamic part and a stationary part that includes extremely small spatial deviations. Such a decomposition was found to be applicable for the simulation of low-Mach-number thermally driven flows, as it provides the same order of magnitude for all the terms in the momentum and energy equations and eliminates acoustic waves. Significant progress in this field may be attributed to the works [3–5] and to the study [6], which employed algorithms based on finite differences and spectral methods, respectively, for the simulation of non-Boussinesq natural convection confined flows. A weakly compressible approximation was used in further simulations of numerous non-Boussinesq natural convection flows [7–14] to address various problems in physics and computational science. The common drawback of all weakly compressible approximations is that the results obtained for flows with a dominant hydrodynamic part (e.g., high velocity flows) maybe inaccurate, which means that a fully compressible approach must be used.

Fully compressible approximations for low-Mach-number flows typically employ either density-based or pressure-based solvers. Although density-based formulations were traditionally utilized for simulating high-speed compressible flows (neglecting viscous effects), efforts have been made to extend the applicability of these formulations to configurations in which viscous effects play a significant role. These configurations include laminar natural convection compressible flows [7, 15, 16], low-Mach-number injection flows [11], and natural convection flows in a laminar-turbulent transition regime [17]. A key feature of density-based solvers is that continuity, momentum, and all other transport equations are first solved in a fully coupled manner, and the pressure field is then derived from an equation of state. As a result, the coupled operator is typically ill conditioned when applied to low-Mach-number flows, whose treatment requires sophisticated numerical techniques, such as preconditioning and dual-time stepping. When the simulations are performed on high-resolution grids or applied to 3D flows, density-based solvers typically suffer from a slow convergence rate and produce results with low accuracy. Pressure-based solvers offer a better alternative for the simulation of fully compressible natural convection flows. In pressure-based solvers, the calculation of the pressure is separated from that of the velocity field. In the first step, the pressure field is taken from the previous time step and the momentum equations are solved, thereby yielding the velocity field, which does not satisfy the continuity equation. In the second stage, a pressure-correction equation

(which is derived from the continuity equation) is solved. Thereafter, the pressure and the velocity components are corrected to meet the continuity constraint. Finally, the solution of the pressure-correction equation is followed by the solution of the energy equation and updating of the density and the viscosity fields by relying on the equations of state and Sutherland equations. Typically, outer iterations are needed to achieve convergence of the velocity, the temperature, and the density fields and to satisfy the continuity constraint. Despite the fact that the pressure-based approach (employing either fractional-step or SIMPLE methods) is well documented in the literature [18, 19], numerical simulations of fully compressible natural convection in enclosures performed by utilizing the above algorithm are quite scarce, with the prominent exceptions of the studies of Sewall and Tafti [20] and Barrios-Pina et al. [21]. In [20], a variable property algorithm based on the fractional-step method was developed to simulate transient natural convection flows in the presence of large temperature differences without using the low-Mach-number assumption. The algorithm was then adopted in [21] to conduct a thermodynamic analysis aimed at determining the contribution of each term in the total energy equation.

In practice, most realistic engineering applications involving confined natural convection flow are characterized by complex geometries, which can significantly challenge the accuracy of the calculated flow properties. For these applications, the immersed boundary method (IBM), initially developed by Peskin [22], may be used as a convenient tool to simulate the flow in the presence of complex boundaries while maintaining an acceptable level of accuracy. The IBM can simulate flow around complex, movable, and deformable boundaries. The simulations take advantage of solvers utilizing compact and simple stencils of discretized differential operators that can be efficiently employed on structured grids or solvers based on the Lattice Boltzmann method (see e.g [23]). No-slip boundary conditions and prescribed values of the temperature (or heat flux) on each immersed boundary are enforced by introducing forces and heat fluxes as additional unknowns in the problem. Closure of the overall system is achieved by including additional equations in the form of kinematic constraints for all the unknowns.

In the past decade, the IBM has been widely utilized for investigating natural convection within enclosures with embedded discrete thermally active sources (or sinks) of various geometries. Interest in this field was generated by its relevance to a broad spectrum of engineering applications based on gas-solid heat exchangers and a need to investigate the instability characteristics of highly separated confined flows. Worth mentioning in this context are the works [24–27] and the studies [28–32] that addressed natural convection confined flows in the presence of bodies of complex two- and three-dimensional geometries, respectively.

Studies utilizing the IBM for the analysis of thermal compressible flows are relatively scarce. Most of the works in this field either address high-Mach-number compressible flows, focusing on transonic/supersonic transitions, or compare the characteristics of subsonic flows with those of supersonic flows. For high-Mach-number flows, the impacts of viscosity and the thermal behavior of the flow are negligible compared to the compressibility effects, and thus both phenomena have typically been neglected when simulating high-Mach-

number flows. In contrast, in the simulation of low-Mach-number thermally driven flows – the focus of the current study – both effects play a significant role and should be carefully addressed.

It should be noted that an accurate implementation of IBM forcing in low-Mach-number compressible flows is still the subject of active research. In a recently developed IBM scheme [33], Riahi et al. introduced a novel pressure-based correction of IBM forcing (in addition to the classical one based on the time derivative of velocity)* and applied it to the analysis of three-dimensional low- and high-Mach-number pressure driven flows. Comparison of the obtained results with the corresponding data obtained by body-fitted numerical simulations revealed that pressure correction of IBM forcing significantly improved the accuracy of the IBM procedure for low-Mach-number flows. An additional contribution to the IBM for the simulation of compressible thermally driven confined flows was made by Kumar and Natarajan [33], who developed a diffuse immersed boundary method for thermally driven non-Boussinesq flows. However, the method relies on a low-Mach-number approximation that treats the governing equations as quasi-incompressible and therefore cannot be considered as a fully compressible approach.

The present study thus aims to develop and extensively verify a general transient pressure-based formulation for the simulation of thermally driven non-Boussinesq flows within complex geometries. The simulations are performed by utilizing second-order backward finite difference and standard second-order finite volume methods [35] for the temporal and spatial discretizations, respectively. To the best of our knowledge, the current work is a first of its kind in which the pressure-based correction IBM, originally developed for compressible pressure driven flows [33], has been successfully incorporated into a fully compressible pressure-based natural convection solver utilizing a semi-implicit fractional-step algorithm.

2 Theoretical background

2.1 Physical model

Natural non-Boussinesq convection within a rectangular cavity of dimensions $L \times H$ filled with an ideal gas is considered. In the presence of a gravitational field $-g\hat{j}$, the flow is driven by the temperature difference between the cold boundaries of the cavity and the hot surface of a cylinder located at the geometrical center of the cavity, as shown in Fig.1. The left (LW), right (RW), top(TW) and bottom (BW) walls of the cavity are maintained at a constant cold temperature T_c, while the surface of the cylinder (CL) is maintained at a constant hot temperature T_h. For the most general case in which the temperature difference $T_h - T_c$ is not restricted to small values, the natural convection flow generated within the cavity is fully compressible.

The flow is governed by a set of non-dimensional continuity, momentum, and energy

*We note in passing that pressure correction of the direct forcing IBM must not be confused with a pressure-correction equation of fractional-step- and the SIMPLE-related methods.

Figure 1: Geometry and boundary conditions for a cold cavity with a hot cylinder at the center.

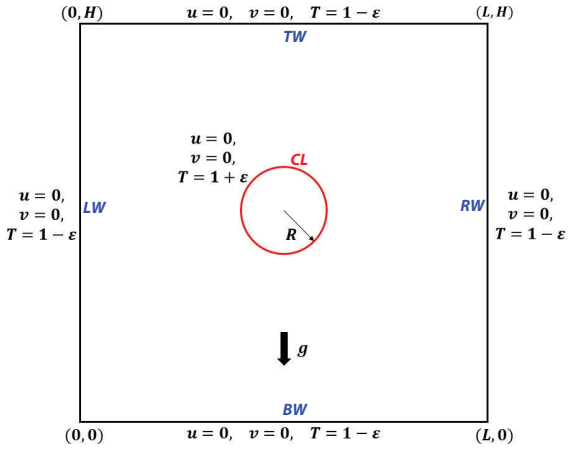

equations:

$$\frac{\partial \rho}{\partial t} + \nabla \cdot (\rho \vec{u}) = 0, \tag{2.1}$$

$$\frac{\partial (\rho \vec{u})}{\partial t} + \nabla \cdot (\rho \vec{u} \otimes \vec{u}) = -\frac{RaPr}{2\varepsilon} \rho \hat{j} - \frac{1}{\kappa M_0^2} \nabla p + Pr \nabla \cdot \left(\mu \left[(\nabla \vec{u} + \nabla \vec{u}^T) - \frac{2}{3} (\nabla \cdot \vec{u}) \bar{\bar{I}} \right] \right) + \vec{f}^{\Gamma}, \tag{2.2}$$

$$\frac{\partial (\rho C_p T)}{\partial t} + \nabla \cdot (\rho \vec{u} C_p T) = \nabla \cdot (k \nabla T) + \frac{\kappa - 1}{\kappa} \left(\frac{\partial p}{\partial t} + \vec{u} \cdot \nabla p \right) + q^{\Gamma}, \tag{2.3}$$

$$\rho = \frac{p}{T} = C_\rho p. \tag{2.4}$$

where $\vec{u}(u,v), p, T, \rho, \mu, k, C_p, \kappa, C_\rho$ are the non-dimensional velocity, pressure, temperature, density, dynamic viscosity, thermal conductivity, specific heat capacity at constant pressure, ratio of specific heat capacities and density coefficient, respectively, and $\bar{\bar{I}}$ is the unity matrix. The impact of the immersed cylinder on the surrounding flow is addressed by introducing the source terms $\vec{f}^{\Gamma}, q^{\Gamma}$ corresponding to the volumetric force and heat source, respectively. Note that in accordance with the IBM formalism as detailed in section 2.2, Eqs. (2.1-2.4) are solved on the whole computational domain including the cylinder interior.

Eqs. (2.1-2.4) are rendered dimensionless using the characteristic scales L_0 for length, L_0^2/α_0 for time, α_0/L_0 for velocity, p_0 for pressure, ρ_0 for density, T_0 for temperature, C_{p_0} for specific heat capacity at a constant pressure, μ_0 for dynamic viscosity, k_0 for thermal conductivity and α_0 is thermal diffusivity. The dimensionless groups governing the flow under consideration are the Rayleigh number (Ra), the Prandtl number (Pr), the Mach number (M_0) and the normalized temperature difference parameter (ε) defined as:

$$Ra = \frac{\rho_0 g (T_h - T_c) L_0^3}{\mu_0 \alpha_0 T_0}, \; Pr = \frac{\mu_0}{\rho_0 \alpha_0}, \; M_0^2 = \frac{\alpha_0^2 / L_0^2}{\kappa R T_0}, \; \varepsilon = \frac{T_h - T_c}{T_h + T_c} = \frac{T_h - T_c}{2T_0} \tag{2.5}$$

Note that despite the fact that the value $T_h - T_c$ is included in the definition of Ra and ε , the two parameters are independent of each other and can be changed separately. The Sutherland law determining the dependence of both the viscosity and the thermal conductivity values on temperature is applied, giving:

$$\mu = \frac{1+C_\mu}{T+C_\mu} T^{3/2}, \tag{2.6}$$

$$k = \frac{1+C_k}{T+C_k} T^{3/2}, \tag{2.7}$$

where C_μ, C_k are the Sutherland non-dimensional temperatures for viscosity and thermal conductivity included in the governing Eqs. (2.2-2.3).

2.2 IBM for thermal compressible flow

To enforce the kinematic constraints of no-slip and of the prescribed temperature value on the surface of the embedded cylinder, the IBM is employed when solving momentum and energy equations. To impose the kinematic constraints, the IBM utilizes regular (typically Cartesian) Eulerian grids by introducing a set of additional volumetric forces and heat sources on the surface of the immersed body, which is described by a discrete set of Lagrangian points. The current study extends the pressure-corrected direct forcing IBM presented in [33] – originally developed for compressible isothermal flows – to the simulation of non-Boussinesq natural convection flows. Similarly to the conventional direct forcing IBM, the formulation developed here incorporates interpolation and regularization operators facilitating an exchange of data between Eulerian and Lagrangian grids and a procedure enabling the direct calculation of the Lagrangian volumetric heat and force sources.

2.2.1 Interpolation

The interpolation step transfers quantities (e.g., $(\rho\vec{u}), (\rho C_p T), (\nabla p)$) from the Eulerian mesh to the points determining the Lagrangian surface ∂B. The procedure employs an interpolation operator I defined as:

$$I[\vec{\boldsymbol{u}}_{\boldsymbol{E}} + \vec{\boldsymbol{v}}_{\boldsymbol{E}}]_{\vec{X}_L} = \vec{\boldsymbol{U}}_{\boldsymbol{L}} + \vec{\boldsymbol{V}}_{\boldsymbol{L}} = \sum_{i \in N_x \, j \in N_y} (\vec{\boldsymbol{U}}_{\boldsymbol{L}} + \vec{\boldsymbol{V}}_{\boldsymbol{L}})_{i,j}^{N_x, N_y} \delta(x_i - X_L) \delta(y_j - Y_L) \Delta x \Delta y \tag{2.8}$$

where $\vec{\boldsymbol{u}}_{\boldsymbol{E}}(\rho\vec{u}, \rho C_p T), \vec{\boldsymbol{v}}_{\boldsymbol{E}}(\nabla p, 0)$ are physical properties calculated on a Eulerian $N_x \times N_y$ grid, while $\vec{\boldsymbol{U}}_{\boldsymbol{L}}(\rho_L \vec{U}_L, \rho_L C_{p_L} T_L), \vec{\boldsymbol{V}}_{\boldsymbol{L}}(\nabla P_L, 0)$ are the corresponding counterparts calculated on a Lagrangian grid, and δ is a discrete Dirac delta function defined below. Note that we used a bold vector notation to distinguish between the interpolated terms yielded by the solution of momentum or energy equation. From the different smeared approximations of the delta functions, we chose the function described by Roma et al. [36], which was

specifically designed for use on staggered grids, where even/odd de-coupling does not occur. This approximation is expressed as:

$$\delta(r)=\begin{cases}\frac{1}{3\Delta r}\left(1+\sqrt{-3\left(\frac{|r|}{\Delta r}\right)^2+1}\right) & \text{for } |r|\leq 0.5\Delta r,\\ \frac{1}{6\Delta r}\left(5-3\frac{|r|}{\Delta r}-\sqrt{-3\left(1-\frac{|r|}{\Delta r}\right)^2+1}\right) & \text{for } 0.5\Delta r\leq |r|\leq 1.5\Delta r,\\ 0 & \text{otherwise,}\end{cases} \tag{2.9}$$

where Δr is the cell width in the r direction. It is noteworthy that the chosen discrete delta function is supported over three cells. No significant differences in the results are to be expected if other discrete delta functions are used [37].

2.2.2 Direct forcing

After completing the interpolation step, the Lagrangian volumetric forces and heat sources are calculated as suggested in [33]:

$$\vec{F}_L=\frac{1}{\Delta t}(\vec{U}_L^d-\vec{U}_L)-(\vec{V}_L^d-\vec{V}_L)\cdot\hat{n}_{ns} \tag{2.10}$$

where $\vec{F}_L(\vec{F}_L,Q_L)$ is a direct forcing term consisting of the volumetric force and heat sources, respectively, the superscript d denotes the kinematic constraints imposed on the surface of the immersed body and $\hat{n}_{ns}$ is a unit vector in the direction perpendicular to the surface of the immersed body.

2.2.3 Regularization

The regularization step smears the values of the volumetric sources calculated at the Lagrangian points back to the Eulerian grid. The procedure is implemented by utilizing the same delta functions as in the interpolation step. The values of the volumetric force and heat source terms evaluated on the Eulerian mesh by utilizing the regularization operator R are given by:

$$\vec{f}^{\Gamma}(x,y)=R[\vec{F}_L]_E=\sum_{L\in N_L}\vec{F}_L\delta(x_i-X_L)\delta(y_j-Y_L)\Delta x\Delta y \tag{2.11}$$

where $\vec{f}^{\Gamma}(x,y)(\vec{f}^{\Gamma}(x,y),q^{\Gamma}(x,y))$ is the Eulerian direct forcing term consisting of the volumetric force and heat sources.

3 Numerical methodology

The flow is governed by a system of continuity, momentum, and energy equations, which are solved numerically. This study utilizes the fractional-step method, which separates

the calculation of the pressure field from the calculation of the velocity field at each time instance. When utilized in the context of the Boussinesq approximation (i.e., the flow is assumed to be incompressible), the method consists of a number of basic steps employed at each time instance: (i) the predictor step aimed at the estimation of the non-solenoidal velocity field by utilizing the pressure field from the previous time step; (ii) the corrector step aimed to obtain the pressure correction for the current time step; (iii) the projection step using the pressure-correction values to update the pressure field and to project the velocity field on the divergence free subspace; and (iv) solution of the energy equation. For non-Boussinesq (i.e., fully compressible) natural convection flows, the procedure is more complicated [18], since in that case the pressure constitutes a thermodynamic property rather than a simplified hydrodynamic property. An additional difficulty is that for compressible flows under realistic conditions, density, viscosity, and thermal conductivity are not constant. The flow around a body of complex geometry is resolved by employing the direct forcing IBM applied to compressible flow, and the velocity, pressure, and temperature kinematic constraints to be enforced on the surface of the immersed body. The methodology and the numerical formulation incorporating a pressure-corrected IBM into a semi-implicit fractional-step method developed for the simulation of natural convection flow around complex geometries is presented below.

3.1 Computational procedure

In this section the details on implementation of fractional step method to satisfy the continuity equation and the IBM formalism to satisfy the kinetic constraints on the syrface of the immersed body are given. Note that the second order backward finite difference and standard second order finite volume method [35] was used for the temporal and the spatial discretizations, respectively.

3.1.1 Predictor step

$$\begin{aligned} \frac{3\rho^{m-1}\vec{u}^*}{2\Delta t} - Pr\nabla\cdot\left(\mu^{m-1}\left[(\nabla\vec{u}+\nabla\vec{u}^T)-\frac{2}{3}(\nabla\cdot\vec{u})\bar{\bar{I}}\right]^{*/n}\right. = \\ = -\frac{RaPr}{2\varepsilon}\rho^{m-1}\hat{j} - N(\rho^{m-1},\vec{u}^n) - \frac{1}{\kappa M_0^2}\nabla p^{m-1} + \frac{4(\rho\vec{u})^n-(\rho\vec{u})^{n-1}}{2\Delta t}, \end{aligned} \tag{3.1}$$

where $\vec{u}^*$ is the predicted velocity that has to be calculated on the basis of the velocity field $\vec{u}^n$, known from the previous time step, and on the basis of the density, dynamic viscosity and pressure fields known from the previous outer iteration $m-1$. The purpose of the outer iteration is to impose the continuity constraint on the predicted velocity field $\vec{u}^*$ at the end of the iteration process. The term $N(\rho^{m-1},\vec{u}^n)$ appearing in the right hand side of Eq. (3.1) denotes the non-linear convective terms, so that Eq. (3.1) is solved sequentially for each velocity component. For this reason the second term of the left hand side of Eq.(3.1) contains both terms that are treated implicitly (denoted by * superscript) and explicitly (i.e. taken from the n^{th} time step). This notation was introduced to distinguish

between velocity components corresponding to different directions. That is, the velocity components coinciding with the direction of the corresponding momentum equation are treated implicitly while the velocity components perpendicular to this direction are taken from the previous time step. Note also that for incompressible and Boussinesq flows with constant viscosity, the second term may be simplified to $Pr\nabla^2(\vec{u}^*)$ and treated fully implicitly.

3.1.2 First momentum Corrector

After obtaining the predicted velocity, the pressure-correction equation, which has been derived from the continuity equation, is solved as follows:

$$\frac{3}{2\Delta t}C_\rho p' - \nabla\cdot\left(\frac{2\Delta t}{3\kappa M_0^2}\nabla p'\right) - \nabla\cdot(C_\rho p'\vec{u}^*) = -\Delta\dot{m}^*, \tag{3.2}$$

where $\Delta\dot{m}^*$ is the mass flow imbalance generated because the predicted velocity does not necessarily satisfy the continuity equation:

$$\Delta\dot{m}^* = \frac{3\rho^{m-1} - 4\rho^n + \rho^{n-1}}{2\Delta t} + \nabla\cdot(\rho^{m-1}\vec{u}^*). \tag{3.3}$$

Solution of the pressure-correction equation yields the pressure correction field p' used for calculation of the intermediate pressure:

$$p^* = p^n + p', \tag{3.4}$$

which is subsequently used as a predictor after the presence of the immersed body has been taken into account.

3.1.3 Application of the IBM for velocity to enforce the non-slip kinematic constraint on the surface of the immersed body

After acquiring the intermediate pressure, the IBM for velocity is implemented via Eqs. (2.8-2.11). Note that the term $\vec{f}^\Gamma$ is not recalculated during the outer iteration and is determined only once at the beginning of the time step:

$$\vec{f}^\Gamma = R\left[\frac{\rho_L^{m-1}}{\Delta t}(\vec{u}_L^d - \vec{u}_L^*) - (\nabla p_L^d - \nabla p_L^*)\cdot\hat{\boldsymbol{n}}_{ns}\right]_{\boldsymbol{E}}. \tag{3.5}$$

As a result, the calculated volumetric Eulerian force exerted by the surface of the immersed body is added to the right-hand side of the momentum equation.

3.1.4 Solution of the momentum equation with the impact of the immersed body

After the Eulerian force has been calculated, the momentum equation with an updated right-hand side is solved again to determine the new velocity field that takes into account

the impact of the immersed body:

$$\begin{aligned}\frac{3\rho^{m-1}\vec{u}^m}{2\Delta t}-Pr\nabla\cdot\left(\mu^{m-1}\left[(\nabla\vec{u}+\nabla\vec{u}^T)-\frac{2}{3}(\nabla\cdot\vec{u})\bar{\bar{I}}\right]^{m/n}\right)=\\ =-\frac{RaPr}{2\varepsilon}\rho^{m-1}\hat{\vec{j}}-N(\rho^{m-1},\vec{u}^n)-\frac{1}{\kappa M_0^2}\nabla p^*+\frac{4(\rho\vec{u})^n-(\rho\vec{u})^{n-1}}{2\Delta t}+\vec{f}^{\mathrm{T}}.\end{aligned}\tag{3.6}$$

Similarly to Eq. (3.1), the above equation is solved sequentially for each velocity component. For this reason the second term of the left hand side of Eq.(3.6) contains both terms that are treated implicitly (i.e. the current iteration terms denoted by m superscript) and explicitly (i.e. taken from n^{th} time step). This notation was introduced to distinguish between velocity components corresponding to different directions. That is, the velocity components coinciding with the direction of the corresponding momentum equation are taken from the current iteration and treated implicitly while the velocity components perpendicular to this direction are taken from the previous time step.

3.1.5 Second momentum corrector

At this stage, the pressure-correction equation with the updated right-hand side is solved:

$$\frac{3}{2\Delta t}C_\rho p''-\nabla\cdot\left(\frac{2\Delta t}{3\kappa M_0^2}\nabla p''\right)-\nabla\cdot(C_\rho p''\vec{u}^m)=-\Delta\dot{m}^m,\tag{3.7}$$

where $\Delta\dot{m}^m$ is a mass flow imbalance that arises because the predicted velocity still does not necessarily satisfy the continuity equation, where $\Delta\dot{m}^m$ is given as:

$$\Delta\dot{m}^m=\frac{3\rho^{m-1}-4\rho^n+\rho^{n-1}}{2\Delta t}+\nabla\cdot(\rho^{m-1}\vec{u}^m).\tag{3.8}$$

Next, the new pressure and the intermediate density fields are calculated by:

$$p^m=p^*+p'',\ \rho^*=\rho^n+C_\rho(p'+p'').\tag{3.9}$$

3.1.6 Solution of the energy equation without the impact of the immersed body

We next solve the energy equation:

$$\begin{aligned}\frac{3\rho^*C_pT^*}{2\Delta t}+\nabla\cdot(\rho^*\vec{u}^mC_pT^*)-\nabla\cdot(k^{m-1}\nabla T^*)=\\ =\frac{\kappa-1}{\kappa}\left(\frac{3p^m-4p^n+p^{n-1}}{2\Delta t}+\vec{u}^m\cdot\nabla p^m\right)+\frac{4\rho^nC_pT^n-\rho^{n-1}C_pT^{n-1}}{2\Delta t}.\end{aligned}\tag{3.10}$$

Note, the T^* field constitutes the intermediate temperature, which was obtained without considering the presence of the immersed body.

3.1.7 Application of the IBM to enforce a given temperature on the surface of the immersed body

At each time step in the first correction iteration, the IBM for temperature is implemented via Eqs. (2.8-2.11) after acquiring the intermediate temperature. Note that the term q^{Γ} is not recalculated during the outer iteration and is determined only once at the beginning of the time step:

$$q^{\Gamma} = R\left[\frac{\rho_L^* C_p}{\Delta t}(T_L^d - T_L^*)\right]_{\boldsymbol{E}}. \tag{3.11}$$

As a result, the calculated volumetric Eulerian heat source exerted by the surface of the immersed body is added to the right-hand side of the energy equation.

3.1.8 Solution of the energy equation with the impact of the immersed body

We next solve the energy equation:

$$\begin{aligned} &\frac{3\rho^* C_p T^m}{2\Delta t} + \nabla\cdot(\rho^* \vec{u}^m C_p T^m) - \nabla\cdot(k^{m-1}\nabla T^m) = \\ &= \frac{\kappa-1}{\kappa}\left(\frac{3p^m - 4p^n + p^{n-1}}{2\Delta t} + \vec{u}^m\cdot\nabla p^m\right) + \frac{4\rho^n C_p T^n + \rho^{n-1} C_p T^{n-1}}{2\Delta t} + q^{\Gamma}. \end{aligned} \tag{3.12}$$

3.1.9 Updating the thermophysical properties

After the energy equation has been solved, the viscosity μ_{ij}^m, the thermal conductivity k_{ij}^m, the coefficient C_ρ, and the density ρ_{ij}^m are updated by using the Sutherland equations (2.6),(2.7) and the equation of state (2.4).

3.1.10 The outer iteration loop

The general formulation of the fully compressible semi-implicit fractional-step method with the embedded IBM governed by Eqs. (3.2),(3.4-3.12) constitutes the outer iteration loop that is employed at each time step. At the end of the iteration, after updating the thermophysical properties, the solver performs a mass conservation check based on the value of the L-infinity norm calculated for the difference between the values of p,ρ and $\vec{u}$ fields in the current and previous iterations. The outer iteration terminates after the value of 10^{-6} of the L-infinity norm has been reached for each field and the simulation proceeds to the next time step by assigning $\vec{u}^{n+1} = \vec{u}^m$,$p^{n+1} = p^m$,$T^{n+1} = T^m$ and $\rho^{n+1} = \rho^m$. To sum up, we present a flowchart (see Fig. 2 summarizing the sequence of stepst hat must be taken to calculate all the flow fields at a given time step with and without an immersed body. It can be seen that the flow simulation involving an immersed body requires additional steps to explicitly calculate the volumetric forces and heat fluxes necessary to satisfy the kinematic constraints on the surface of the body.

Figure 2: Block diagram of the algorithmic sequence required to calculate all the flow fields at a given time step: to the left – without immersed body; to the right – with immersed body.

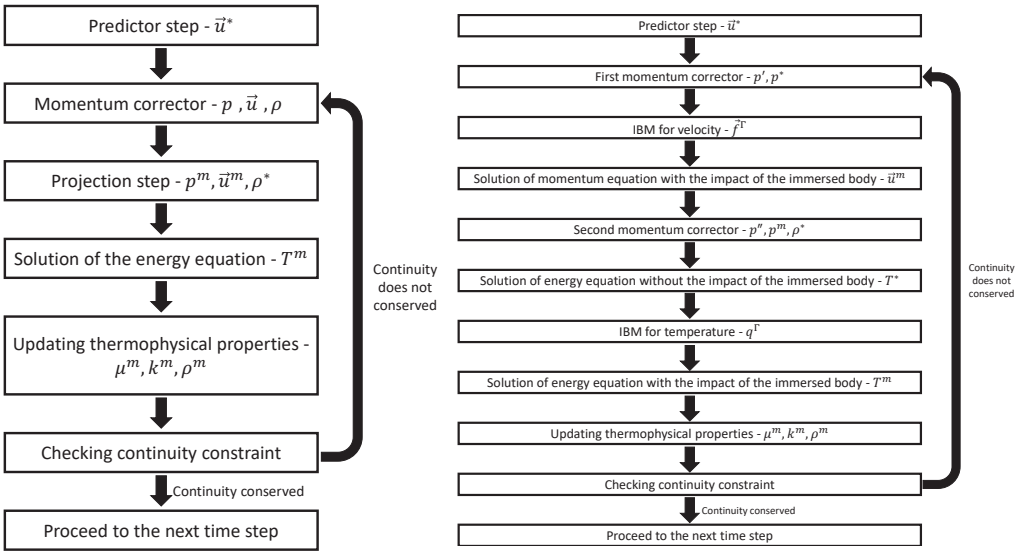

3.2 Solution of the discretized momentum, pressure-correction and energy equations

As a result of the non-constant density ρ and the dependence of the dynamic viscosity μ and the conduction coefficient k on the temperature typical of the fully compressible flow, the discretized momentum, pressure correction, and energy equations contain time varying coefficients. Therefore, the strategies for reaching an efficient solution of the discretized equations should be chosen with care. In the current study, two different strategies, one based on an iterative solution and the other based on a direct solution of the discretized governing equations, were investigated.

The iterative solution utilized the bi-conjugate gradient stabilized (BiCGstab) method [38]. The key idea was to treat only the linear terms of the Helmholtz operator implicitly, while all the non-linear terms were taken either from the previous time step or from the previous iteration. Exploiting the fact that for a 2D problem the Helmholtz operator is built up of 5 non-zero diagonals, we efficiently implemented its product by an arbitrary vector, constituting a major part of the BiCGstab algorithm. However, as is the case for many other iterative methods, the BiCGstab converges up to a certain accuracy, after which it saturates, so that no further decrease of residuals is possible. This limitation can slow down the convergence of the outer iterations, and we therefore sought to eliminate this possible problem by replacing the BiCGstab by the direct method proposed by Lynch et al. [39]. This approach, designated tensor product factorization (TPF) in [39], is based on eigenvalue decompositions (EVDs) of one-dimensional derivative operators and can be applied for the direct inverse of the Helmholtz operators in rectangular domains. Vitoshkin

& Gelfgat [40] demonstrated the computational efficiency of the TPF method for 2D and 3D natural convection benchmark problems by applying the Boussinesq approximation and showed that for fine grids and large Grashof numbers it yields computationally faster time steps than BiCGstab or multigrid iterations. Additionally, it can easily be observed that after application of the TPF solver the relative residual remains below 10^{-12}.

Unfortunately, the EVD method cannot be implemented directly into the correction equations (3.2) and (3.7), because the coefficients of the Helmholtz-like differential operator are not constants. Thus, to apply the EVD solver, all the governing equations should be reformulated. For example, Eq. (3.7) is modified into:

$$\frac{3}{2\Delta t}\overline{C_\rho}p''^{,m}-\nabla\cdot\left(\frac{2\Delta t}{3\kappa M_0^2}\nabla p''^{,m}\right)=-\Delta\dot{m}^m+\nabla\cdot(C_\rho p''^{,m-1}\vec{u}^*)-\frac{3}{2\Delta t}(C_\rho-\overline{C_\rho})p''^{,m-1}, \quad (3.13)$$

where $\overline{C_\rho}=\Big[(C_\rho)_{min}+(C_\rho)_{max}\Big]/2$ and m is the number of the outer iteration. In this formulation, the left-hand side of Eq. (3.13) is a Helmholtz-like elliptic operator with constant coefficients, whose discretized inverse can be expressed via a one-dimensional EVD of the second-derivative operators [41].

4 Verification study

The methodology described in Section 2 was verified by applying it to the solution of two benchmark problems—simulating incompressible and thermally driven compressible flows, i.e., flows driven by two different mechanisms. For the verification, we chose to simulate the isothermal flow in a long narrow rectangular channel driven by a pressure gradient and the natural convection flow within a differentially heated square cavity driven by a temperature gradient. The results obtained for the two configurations were compared with the data available in the literature.

4.1 Test case I - Isothermal compressible flow in a narrow channel

4.1.1 Test case overview

This test case examines the capability to carefully address incompressible isothermal flow by applying the currently developed methodology for compressible flow. The flow within an extended channel was selected as a computational testbed to minimize the effect of the outflow boundary on the upstream recirculation zones. The schematics of the geometric properties and the boundary conditions of the configuration under consideration are shown in Fig. 3.

The fluid enters the domain at the upper half of the left side, proceeds through the channel, and exits at the right side. No-slip velocity and zero-gradient pressure boundary conditions are applied on all the rigid walls. At the inlet, the vertical component of the velocity is equal to zero; the zero-gradient boundary condition is applied to the pressure

Figure 3: Schematics of the flow within an extended channel.

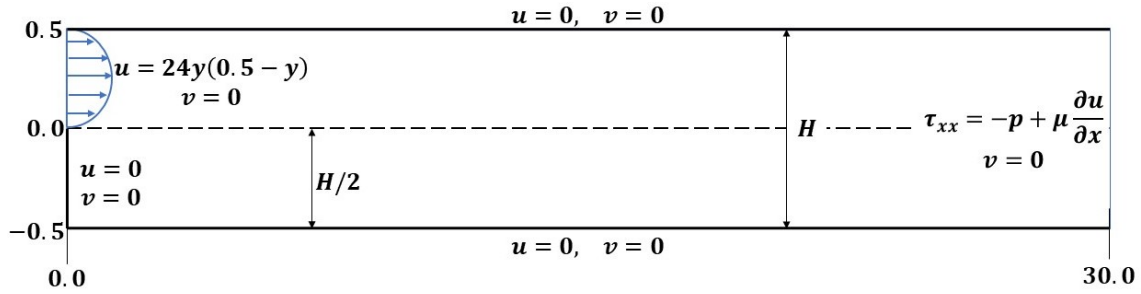

field; and a parabolic distribution with maximal and average values equal to $u_{max}=1.5$ and $u_{avg}=1$, respectively, is assigned to the horizontal velocity component. At the outlet, zero values are set for the normal stress, $\tau_{xx}=-p+\mu\partial u/\partial x$, and for the vertical velocity component. Considering that the pressure field at the outlet is known and is set to zero, the gradient of the horizontal velocity component is also equal to zero.

The non-dimensional continuity and momentum equations and the equation of state governing the flow under consideration are:

$$\frac{\partial\rho}{\partial t}+\nabla\cdot(\rho\vec{u})=0, \tag{4.1}$$

$$\frac{\partial(\rho\vec{u})}{\partial t}+\nabla\cdot(\rho\vec{u}\otimes\vec{u})=-\nabla p+\frac{1}{Re}\nabla\cdot\left(\mu\left[(\nabla\vec{u}+\nabla\vec{u}^{T})-\frac{2}{3}(\nabla\vec{u})\bar{\bar{I}}\right]\right), \tag{4.2}$$

$$\rho=\frac{\kappa M_0^2}{T_0}p, \tag{4.3}$$

where the Reynolds number, Re is based on the average velocity.

4.1.2 Test results and comparison with a benchmark in the literature

The results obtained by the developed methodology were compared to the corresponding data provided in [42] for the value of $Re=800$. Figs. 4-7 present a comparison between the contours of the currently obtained flow fields and the corresponding results reported in [42], which serves as the benchmark for this comparison. As can be seen from Figs. 4-7, the values of all the currently obtained quantities lie in the same range as the corresponding data reported in [42]. The distribution of the streamlines, shown in Fig. 4, along with the distributions of the vorticity and velocity magnitude fields, shown in Figs. 6 and 7, respectively, confirm the presence of staggered low-speed vortices adjacent to the upper and lower walls. The pressure field, shown in Fig. 5, confirms the presence of a "pressure pocket" adjacent to the bottom wall between $x=6$ and $x=7$. As can be seen clearly from Fig. 8, the density variations over the entire domain are insignificant, and the flow can safely be considered as incompressible.

Figure 4: Comparison between the distributions of the streamlines in (a) the current study and (b) the benchmark study [42]. Grid 3000×100.

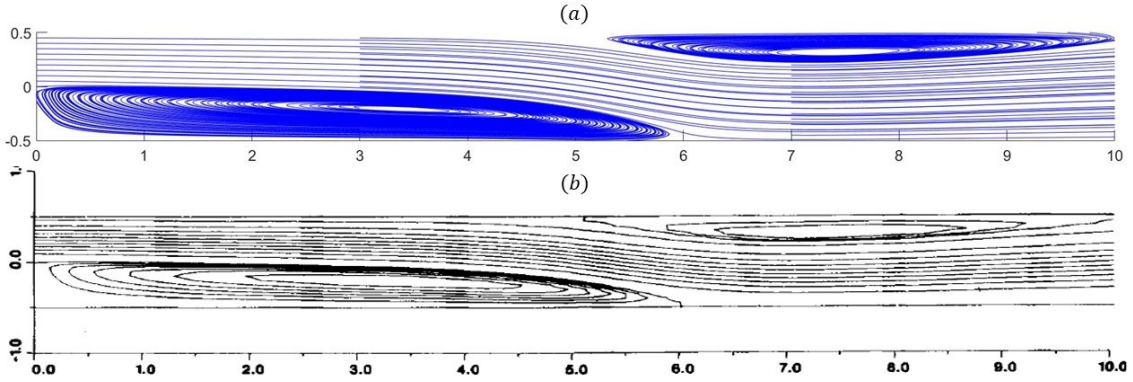

Figure 5: Comparison between the pressure distribution in (a) the current study and (b) the benchmark study [42]. Grid 3000×100.

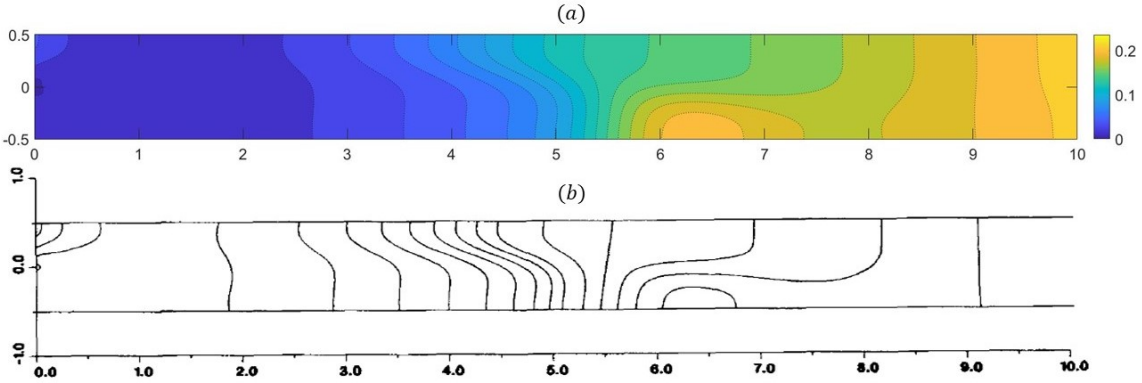

Pressure contours. Level values are 0·01, 0·02, 0·03, 0·04, 0·05, 0·06, 0·07, 0·08, 0·09, 0·10, 0·12, 0·14, 0·16, 0·18, 0·20, 0·22, 0·24

Figure 6: Comparison between the distribution of vorticity in (a) the current study and (b) the benchmark study [42]. Grid 3000×100.

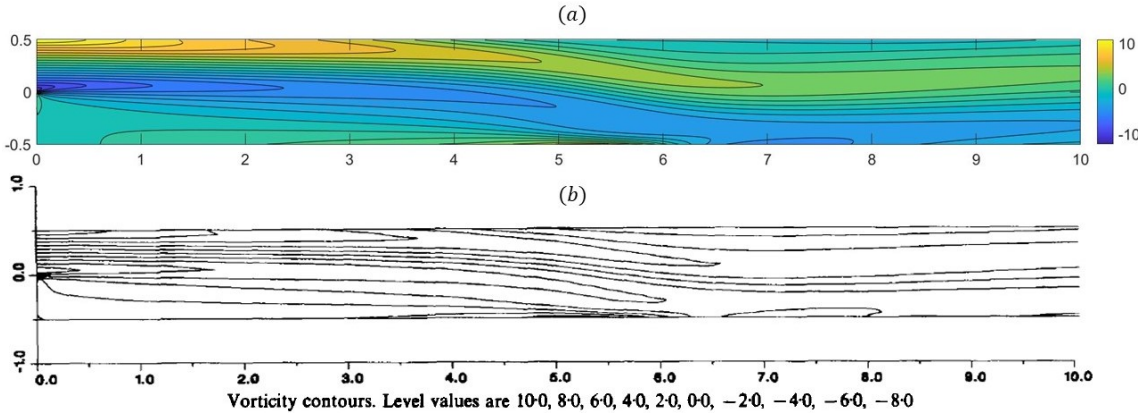

Figure 7: Comparison between the distribution of the velocity magnitude in (a) the current study and (b) the benchmark study [42]. Grid 3000×100.

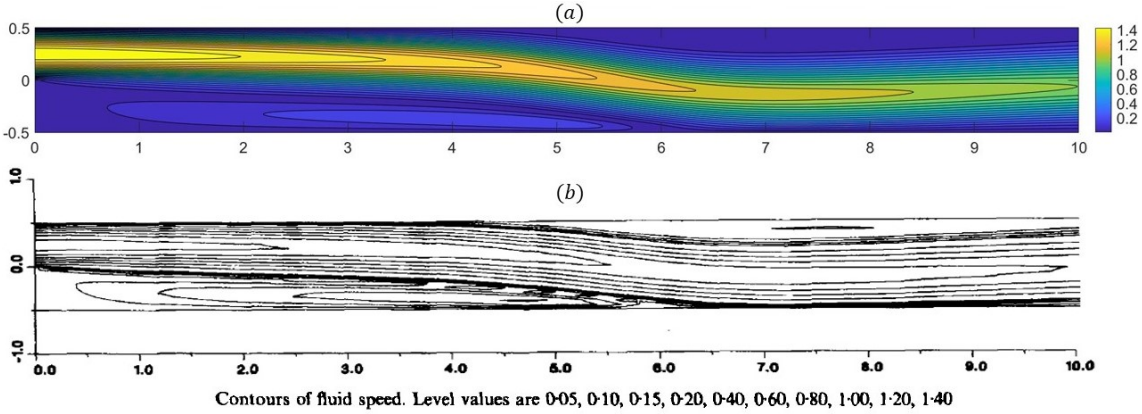

Figure 8: Distribution of the density field. Grid 3000×100.

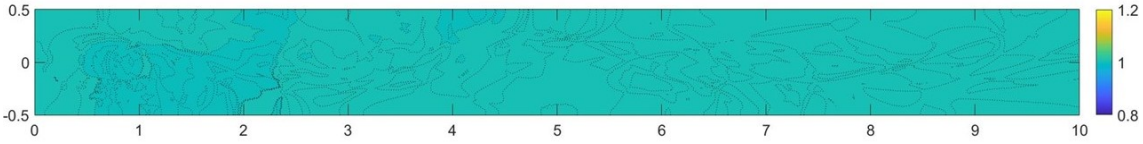

Figs. 9-10 present a comparison between the currently obtained flow characteristics and the corresponding data reported in [42]. A comparison of the pressure and the shear stress distributions along the upper and lower walls of the channel is shown in Fig. 9a and 9b, respectively. A comparison of the currently obtained and benchmark distributions of the horizontal and vertical velocity components, pressure, vorticity, horizontal velocity gradient and normal stress along two vertical lines passing through $x = 7$ and $x = 5$ is presented in Figure 10. All the figures demonstrate the same trends for all the flow characteristics obtained in the current and benchmark studies.

Figs. 9a, 10c and 10f compare the corresponding pressure and the normal stress fields and show excellent agreement between the current and the benchmark values for the two quantities. Acceptable agreement was also obtained for all the other flow characteristics, including the values of both velocity components, the vorticity, and the gradient of the horizontal component of the velocity. An absolute deviation between the values of the above characteristics is limited to 1 percent for the entire range of y coordinates with the exception of the regions in which extremums of the vertical velocity and the gradient of the horizontal velocity are observed. In these regions, the absolute deviation between the current and the corresponding benchmark results is limited to 8 percent.

In summary, the acceptable agreement between the currently obtained and benchmark results for the entire range of flow characteristics verifies the suitability of our numerical methodology for the simulation of almost incompressible flows.

4.2 Test case II - Natural convection flow in a differentially heated cavity

4.2.1 Test case overview

The results presented in this section were obtained by applying the developed methodology to the simulation of compressible natural convection flow in a differentially heated square cavity. The flow is driven by the temperature difference between two vertical walls under the influence of gravity. The obtained flow characteristics were compared with the corresponding independently obtained data [4] that served as the benchmark for this part of our study. The governing equations, characteristic values, and non-dimensional parameters of this flow configuration are presented in Section 2.

The hot and cold walls of the cavity are maintained at constant temperature values of $T_h = 1+\varepsilon$ and $T_h = 1-\varepsilon$, respectively, and are thermally insulated. No-slip and zero gradient boundary conditions are applied for all the velocity components and the pressure, respectively, on all the cavity walls. The schematics summarizing the geometry and boundary conditions of this flow configuration are shown in Fig. 11.

4.2.2 Test results and comparison with a benchmark in the literature

The results obtained in the current study were compared with the corresponding benchmark data reported in [4]. The comparison focused on the distributions of the velocity and the temperature. The data was compared in terms of the values of the vertical temperature stratification parameter θA and the Nusselt number determined by Eqs. (4.4)

Figure 9: Distribution of (a) pressure and (b) shear stress fields along upper and lower channel walls. Grid 3000×100.

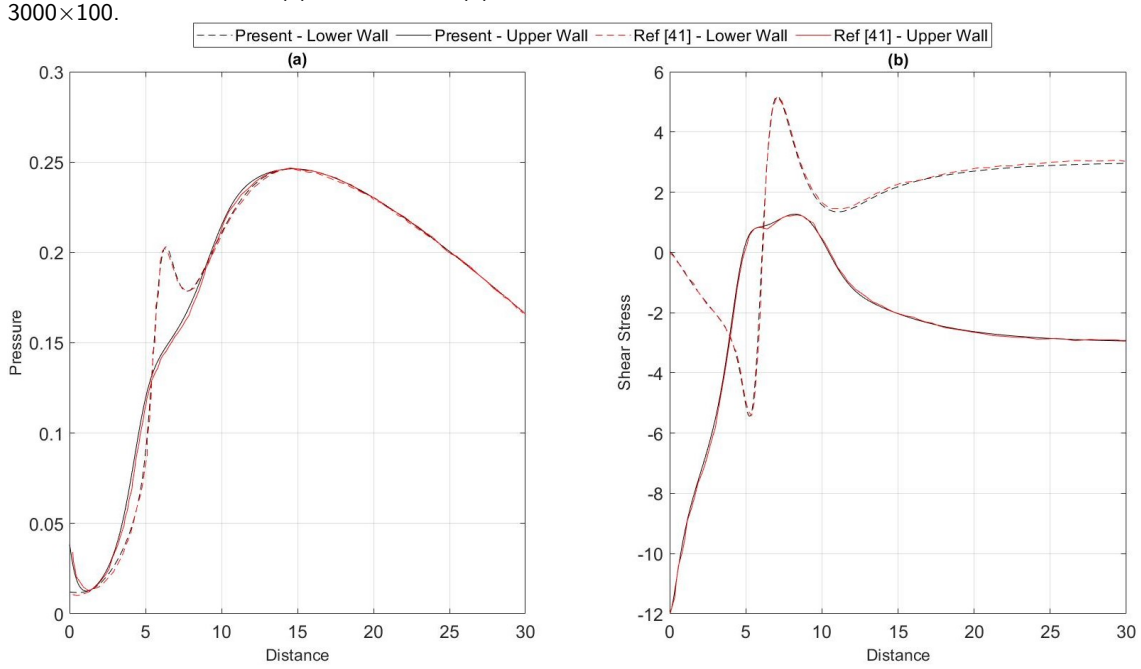

Figure 10: Distribution of: (a) horizontal velocity component; (b) vertical velocity component; (c) pressure; (d) vorticity; (e) horizontal velocity gradient; and (f) normal stress along vertical lines passing through the x=7 and x=15 coordinates. Grid 3000×100.

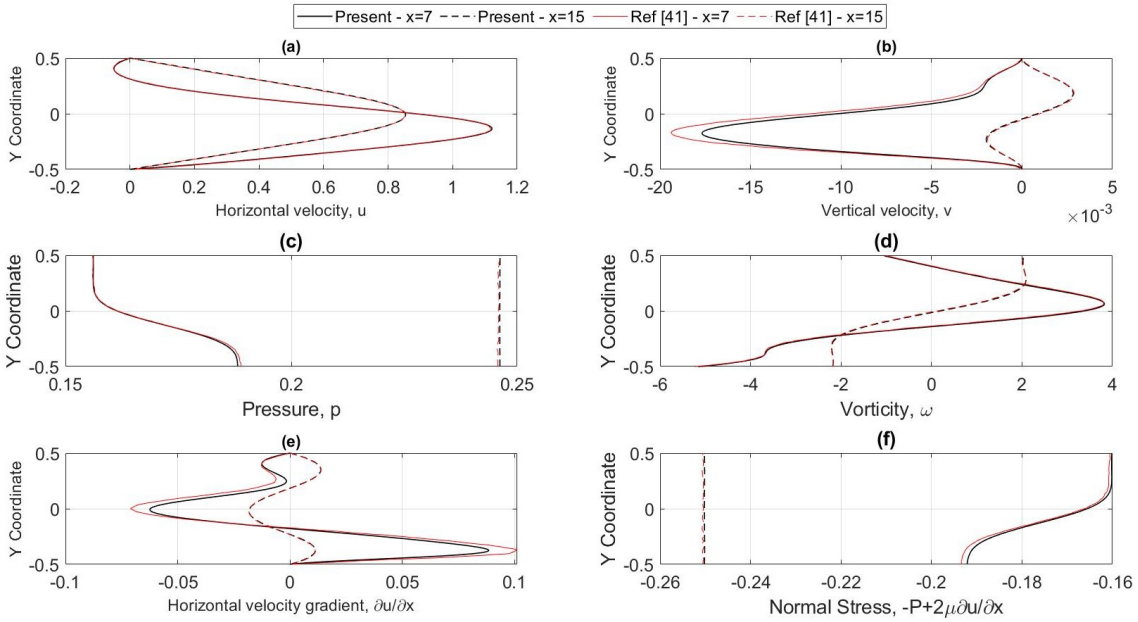

Figure 11: Geometry and boundary conditions of the differentially heated cavity.

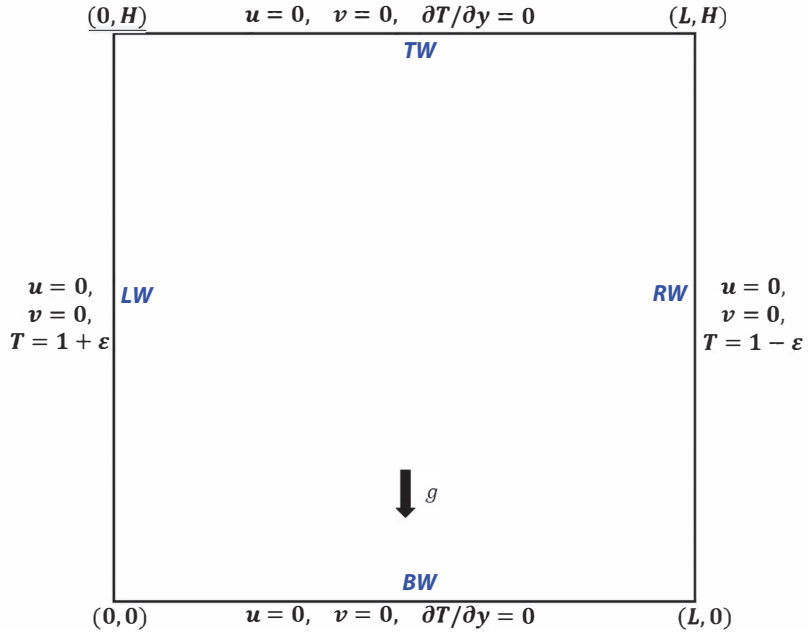

and (4.5), respectively. In accordance with [4], θA was calculated by:

$$\theta A = \frac{AR}{2\varepsilon}\left(\frac{dT}{dy}\right)_{x=\frac{1}{2},y=\frac{1}{2}}, \tag{4.4}$$

where $AR = H/L$ is the aspect ratio.

The average Nusselt number was determined as:

$$\overline{Nu} = -\frac{1}{S}\int_S \frac{k\nabla T}{2\varepsilon} dS, \tag{4.5}$$

where ∇T is the temperature gradient at the wall, and S is the non-dimensional surface area.

In the current study, the Nusselt number was calculated for the hot wall of the cavity. The calculations were performed for the range of $Ra \in [10^3, 10^7]$ and $\varepsilon = 0.005, 0.2, 0.4$ and 0.6. In all the simulations, the value of the aspect ratio $AR = H/L$ was equal to unity. Figs. 12-13 summarize the comparison between our calculations and the benchmark values [4] for the velocity and the temperature fields obtained for the value of $Ra = 10^5$ and the entire range of ε values. Good agreement between the two sets of values can clearly be seen for all the simulations. Note that the temperature and velocity distributions vary with ε. For the lowest value of ε, i.e., $\varepsilon = 0.005$, both the velocity and the temperature distributions are almost skew-symmetric relative to the cavity center and resemble the distributions

Figure 12: Comparison of the contours for $\varepsilon=0.005, Ra=10^5$: (a) velocity, current study, (b) velocity, benchmark study [4], (c) temperature current study, (d) temperature, benchmark study [4].

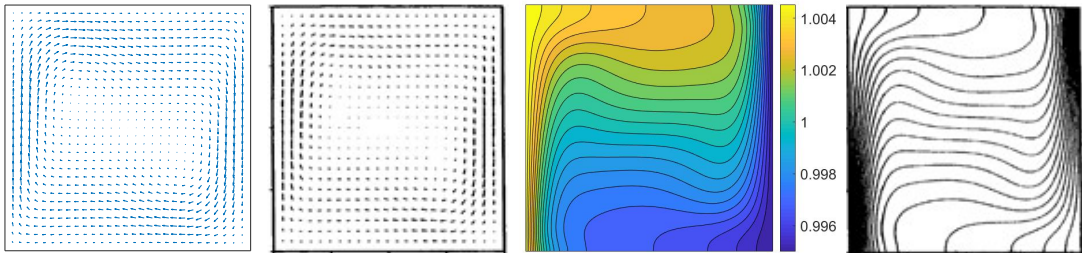

Figure 13: Comparison of the contours for $\varepsilon=0.2, Ra=10^5$: (a) velocity, current study, (b) velocity, benchmark study [4], (c) temperature current study, (d) temperature, benchmark study [4].

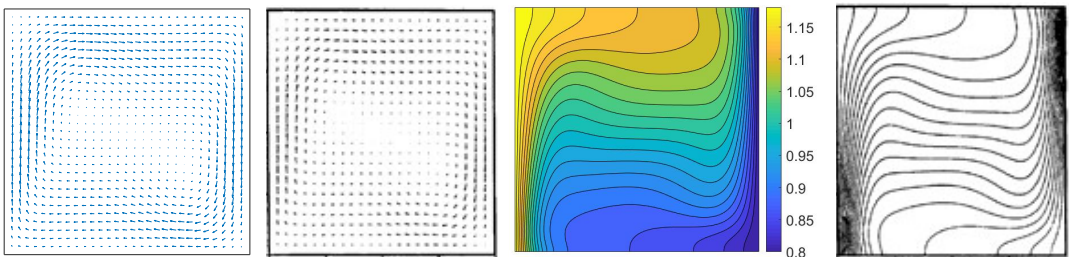

typical of incompressible flows obtained by applying the Boussinesq approximation. With increasing ε values, the flow loses its skew-symmetry as a result of the dependence of its conductivity k and viscosity μ on temperature.

A similar comparison was made for ε constant at its highest value, $\varepsilon=0.6$, and varying Ra over the entire range of Ra values, as shown in Figures 14-19. Good agreement was obtained between our values and the benchmark results [4]. It can clearly be seen that under these conditions the flow is characterized by a breaking of the skew-symmetry relative to the cavity center, even at the lowest value of $Ra=10^3$. For the higher Ra flow regimes dominated by convective heat transfer, the breaking of skew-symmetry becomes

Figure 14: Comparison of the contours for $\varepsilon=0.4, Ra=10^5$: (a) velocity, current study, (b) velocity, benchmark study [4], (c) temperature current study, (d) temperature, benchmark study [4].

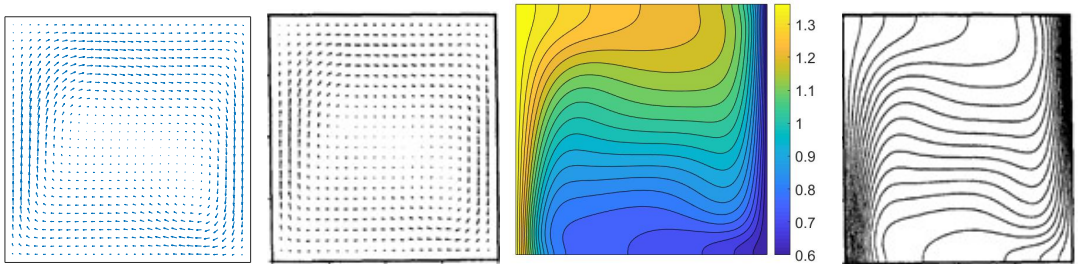

Figure 15: Comparison of the contours for $\varepsilon=0.6, Ra=10^5$: (a) velocity, current study, (b) velocity, benchmark study [4], (c) temperature current study, (d) temperature, benchmark study [4].

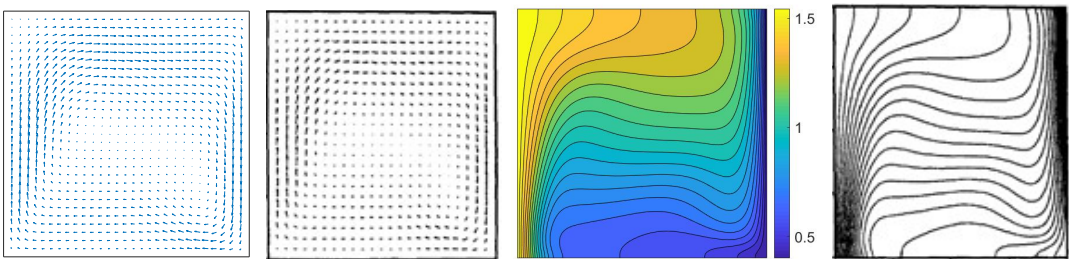

Figure 16: Comparison of the contours for $\varepsilon=0.6, Ra=10^3$: (a) velocity, current study, (b) velocity, benchmark study [4], (c) temperature current study, (d) temperature, benchmark study [4].

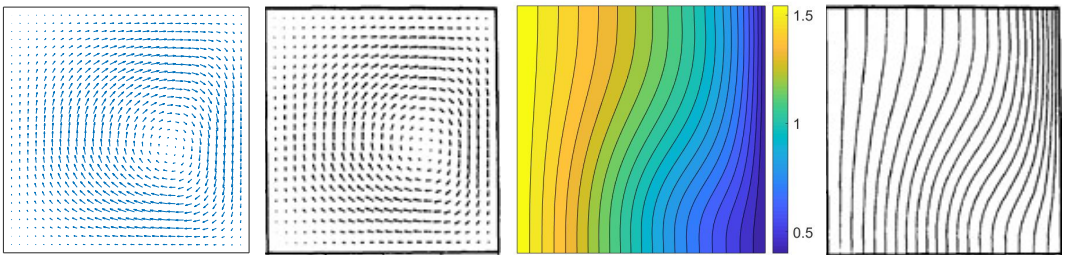

much more pronounced. The breaking of skew-symmetry may be confirmed by examining the differences in the thickness of the boundary layers developing near the hot and cold walls. In fact, the dynamic viscosity of the ideal gas increases with temperature, leading to a thickening of the boundary layer in the vicinity of the hot wall of the cylinder. At the same time, the thickness of the boundary layer decreases close to the cold vertical wall, which, again, is a consequence of a local decrease in viscosity values as a result of the lower temperatures prevailing in this region.

Figs. 20 and 21 present a comparison of our results with the benchmark values [4] for the vertical temperature stratification parameter and the averaged Nusselt number

Figure 17: Comparison of the contours for $\varepsilon=0.6, Ra=10^4$: (a) velocity, current study, (b) velocity, benchmark study [4], (c) temperature current study, (d) temperature, benchmark study [4].

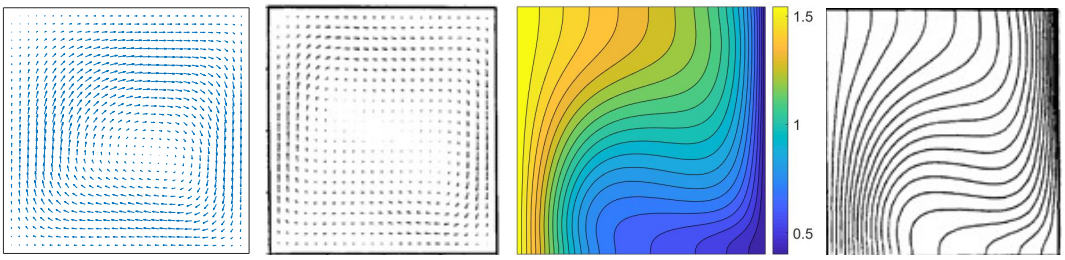

Figure 18: Comparison of the contours for $\varepsilon=0.6, Ra=10^5$: (a) velocity, current study, (b) velocity, benchmark study [4], (c) temperature current study, (d) temperature, benchmark study [4].

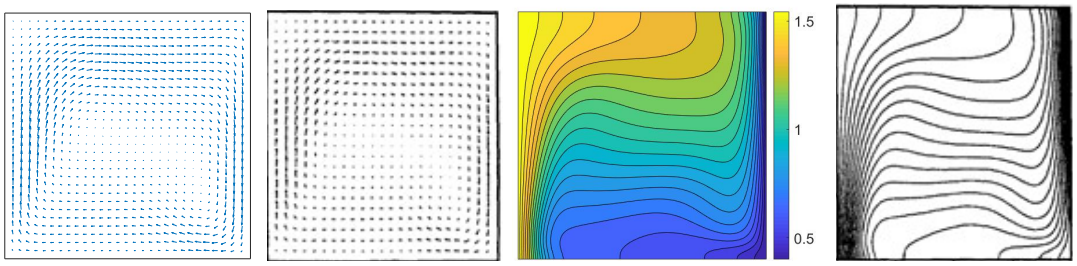

Figure 19: Comparison of the contours for $\varepsilon=0.6, Ra=10^6$: (a) velocity, current study, (b) velocity, benchmark study [4], (c) temperature current study, (d) temperature, benchmark study [4].

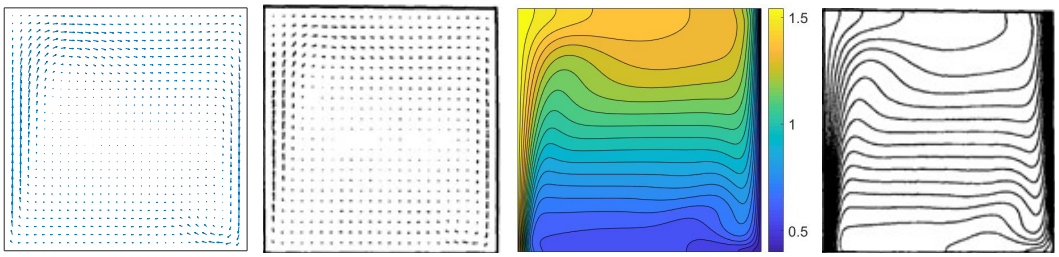

versus Ra values. The simulations were performed on four different grids, namely, two uniform grids of 100×100 and of 200×200 cells, and two non-uniform grids of 100×100 and of 200×200 cells stretched toward the cavity walls to accurately resolve the thinnest boundary layers.

As can be seen from Fig. 20, there was good agreement between our results and the benchmark results [4] for the vertical temperature stratification parameter. Of particular interest was the finding that stretching the grid toward the cavity boundaries was not always the optimal way to increase the accuracy of the results when the values for comparison were acquired close to the cavity center, as can be seen from the θA values obtained on a stretched grid with $\varepsilon=0.005$ and $Ra=10^6$ or a stretched grid with $\varepsilon=0.2$ and $Ra=10^3$. At the same time, asymptotic convergence of the θA values with increasing the grid resolution was clearly observed for both stretched and uniform grids. Fig. 21 demonstrates that the Nu values obtained on the uniform and stretched grids built of 200×200 and 100×100 cells, respectively, showed better agreement with the benchmark results than the corresponding Nu values obtained on the uniform grid built of 100×100 cells, especially for high Rayleigh numbers. Thus, stretching the grid toward the cavity boundaries is the condition of choice when analyzing characteristics based on the temperature gradients at the cavity boundaries.

In summary, the acceptable agreement between our results and those of the benchmark study [4] for the entire range of operating conditions and flow characteristics successfully verifies the suitability of our numerical methodology for the simulation of compressible

Figure 20: Vertical temperature stratification parameter vs. Rayleigh number: comparison of our results with benchmark values [4].

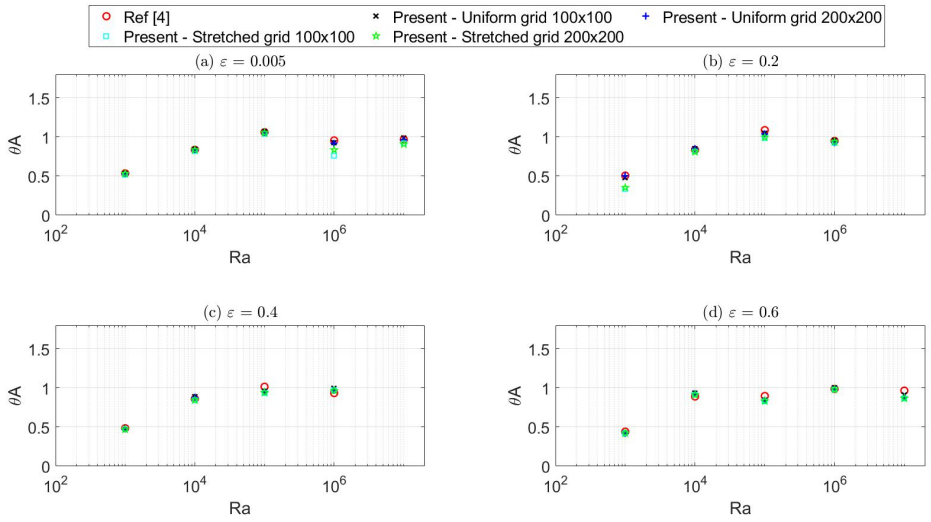

natural convection confined flows.

5 Results and discussion

This section presents the results of a parametric study performed to simulate the natural convection flow developing from the hot surface of a cylinder placed within a square cold cavity (see Fig. 1). The results were obtained for a wide range of governing parameters: $Ra \in \{10^3, 10^4, 10^5, 10^6\}$, $\varepsilon \in \{0.005, 0.2, 0.4, 0.6\}$ and $R/L \in \{0.1, 0.2, 0.3, 0.4\}$. The simulations were performed on two uniform grids having 100 or 200 nodes in each direction, with the time steps of $\Delta t = 10^{-7}$ and $\Delta t = 10^{-8}$, respectively.

The obtained results illustrate changes of the velocity and temperature fields when the temperature-difference parameter ε was varied between 0.005 and 0.6 for the same Ra and R/L values. Additionally, the results were approximated by $Nu - Ra$ power law fits calculated by employing the least-squares technique. The Nusselt number Nu was calculated as is detailed below in subsection 5.2. The Nusselt numbers obtained for the whole range of Ra and for the lowest value of the temperature-difference parameter ($\varepsilon = 0.005$) were compared with the corresponding results available in literature [28], [43] calculated by employing the Boussinesq approximation.

Figure 21: Nusselt number vs. Rayleigh number: comparison of our results with benchmark values [4].

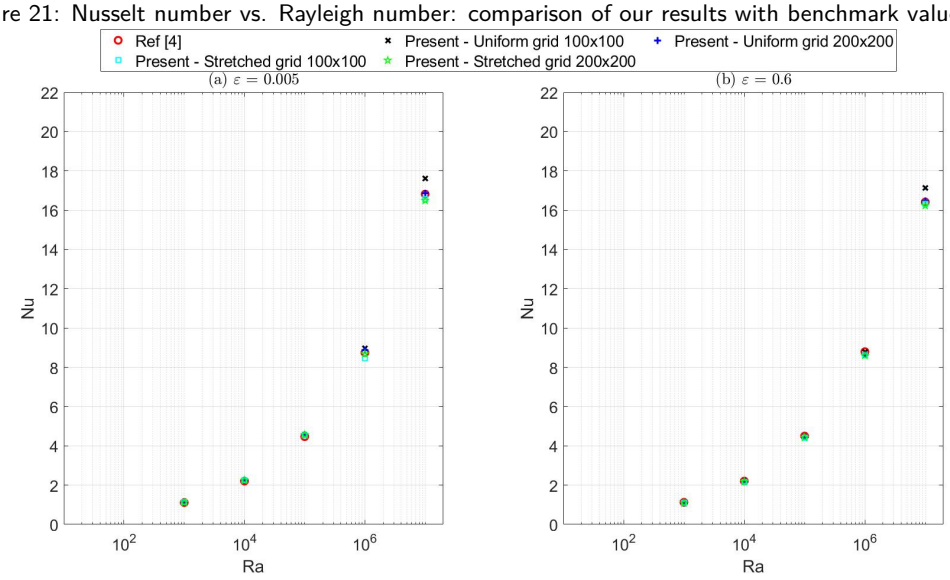

5.1 Qualitative observations

Figs. 22-37 summarize the results in terms of the spatial distribution of the flow path lines and the temperature fields obtained for the values of ε=0.005 and ε=0.6 for the entire range of Ra and R/L values on a uniform grid of 200 cells in each direction. The purpose of this part of the study was to investigate differences between the flow characteristics typical of the lowest ($\varepsilon = 0.005$) and the highest ($\varepsilon = 0.6$) values of the temperature-difference parameter.

Figs. 22-23 and Figs. 30-31 show that for the lowest Rayleigh number, $Ra = 10^3$, there were no significant differences between the spatial distributions of the path lines and the temperature fields, respectively, obtained for the lowest (ε=0.005) and the highest (ε=0.6) values of the temperature-difference parameter, regardless of the cylinder's diameter. The configurations for this Ra number did not contain secondary convective cells, and the temperature distribution was close to linear along the radial direction from the hot cylinder to the cold cavity walls, as may be expected for systems in which conduction constitutes the major heat transfer mechanism. As the Ra value increased, the differences became more visible. Figs. 24-25 and Figs. 32-33, in which the path line and temperature distributions, respectively, are shown for $Ra = 10^4$, showed that the differences in path lines remained insignificant (with no secondary convective cells), but the temperature distribution for the highest value of ε was slightly shifted upwards compared to that observed for the lowest ε value. As for the two highest values of $Ra = 10^5$ and $Ra = 10^6$, the differences between the path line and temperature distributions corresponding to the configurations characterized by the two limit values of ε could be clearly recognized, as may be expected for systems in

Figure 22: Distribution of the path lines for $Ra = 10^3$, $\varepsilon = 0.005$ and $0.1 \leq R/L \leq 0.4$.

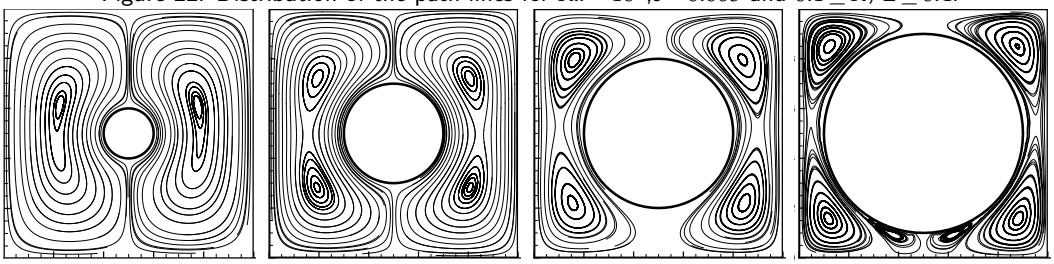

Figure 23: Distribution of the path lines for $Ra = 10^3$, $\varepsilon = 0.6$ and $0.1 \leq R/L \leq 0.4$.

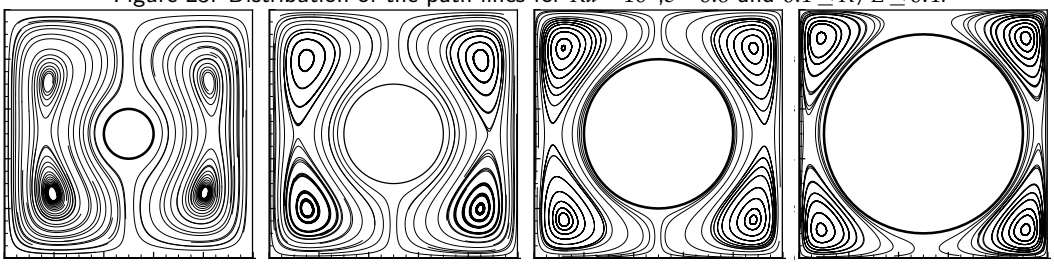

which convection constitutes the major heat transfer mechanism (see Figs. 26-27 and Figs. 34-35). In this range of Ra values, secondary convective cells were sometimes generated, while the temperature distribution along the radial direction was non-linear with clearly recognizable single or multiple thermal plumes rising up from the top of the cylinder.

In summary, secondary convective cells never appeared for $Ra \leq 10^4$ and/or $R/L \leq 0.1$. For $R/L = 0.2$, secondary convective cells appeared only for the value of $\varepsilon = 0.6$ and for the two values of $Ra = 10^5$ and $Ra = 10^6$. For $R/L = 0.3$, secondary convective cells appeared for the two values of $\varepsilon = 0.005$ and $\varepsilon = 0.6$ and the two values of $Ra = 10^5$ and $Ra = 10^6$. For $R/L = 0.4$, secondary convective cells appeared for the two values of ε and only for $Ra = 10^6$. In addition, it was observed that the flows characterized by $\varepsilon = 0.6$ may contain more secondary convective cells than their counterparts characterized by $\varepsilon = 0.005$ - a trend that never occurs the other way around. It thus appears that for flow separation to occur high Ra, R/L and ε values are required simultaneously. It is also noteworthy that an increasing number of secondary convective cells with an increasing value of the Ra number followed the same trend as that observed in Rayleigh-Bénard convection with an increasing aspect ratio, i.e., for high values of R/L, the cylinder curvature can be locally neglected, and the flow in the top region of the cavity resembles the Rayleigh-Bénard configuration.

Figure 24: Distribution of the path lines for $Ra = 10^4, \varepsilon = 0.005$ and $0.1 \leq R/L \leq 0.4$.

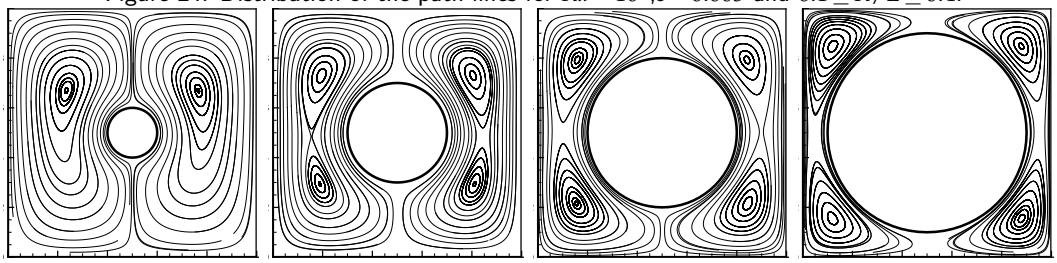

Figure 25: Distribution of the path lines for $Ra = 10^4, \varepsilon = 0.6$ and $0.1 \leq R/L \leq 0.4$.

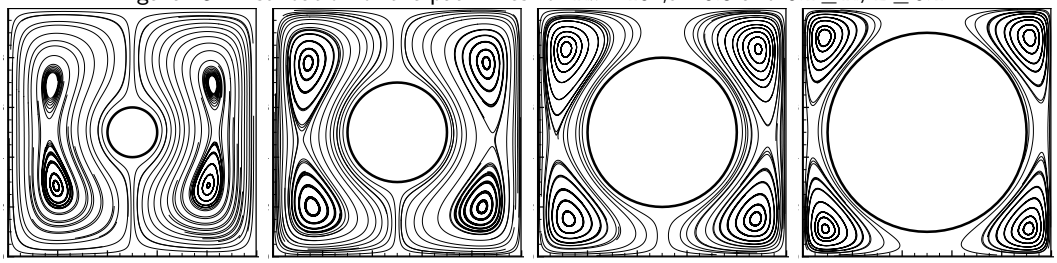

Figure 26: Distribution of the path lines for $Ra = 10^5, \varepsilon = 0.005$ and $0.1 \leq R/L \leq 0.4$.

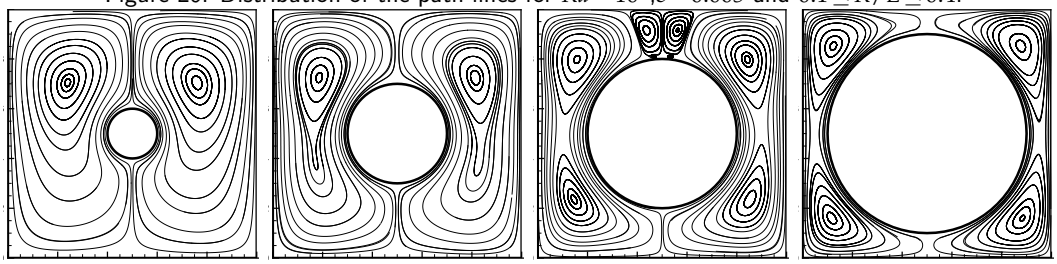

Figure 27: Distribution of the path lines for $Ra = 10^5, \varepsilon = 0.6$ and $0.1 \leq R/L \leq 0.4$.

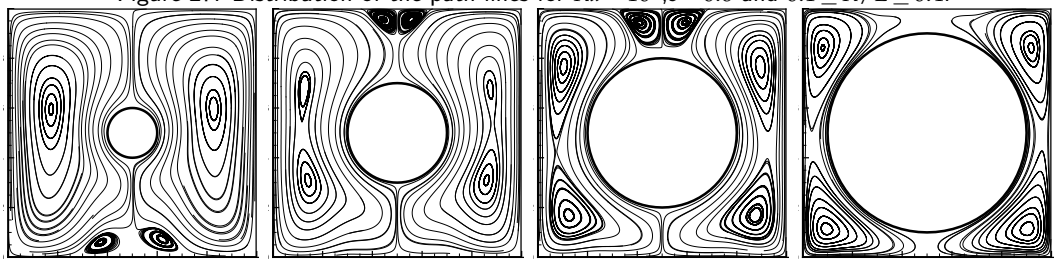

Figure 28: Distribution of the path lines for $Ra = 10^6, \varepsilon = 0.005$ and $0.1 \leq R/L \leq 0.4$.

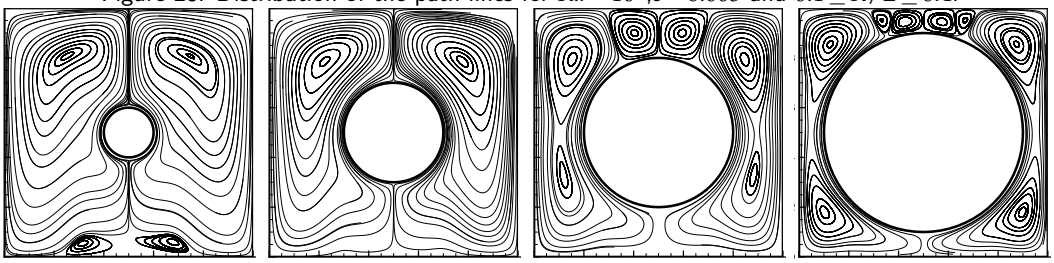

Figure 29: Distribution of the path lines for $Ra = 10^6, \varepsilon = 0.6$ and $0.1 \leq R/L \leq 0.4$.

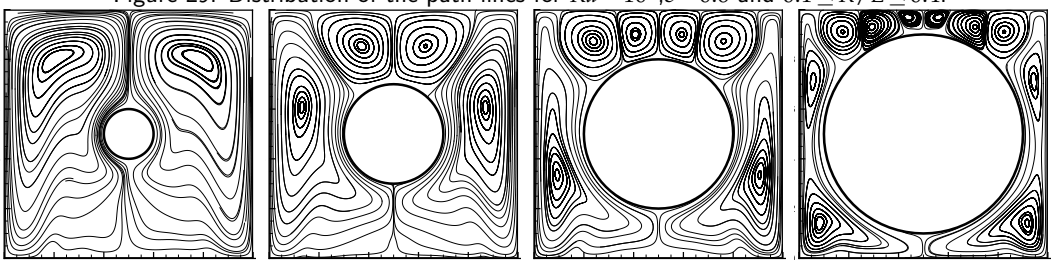

Figure 30: Distribution of the path lines for $Ra = 10^3, \varepsilon = 0.005$ and $0.1 \leq R/L \leq 0.4$.

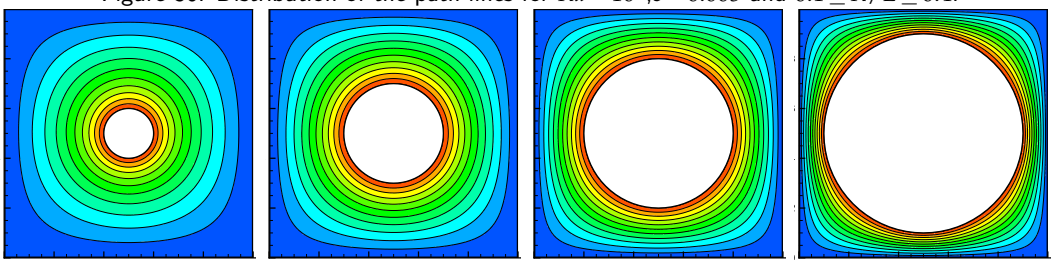

Figure 31: Distribution of the path lines for $Ra = 10^3, \varepsilon = 0.6$ and $0.1 \leq R/L \leq 0.4$.

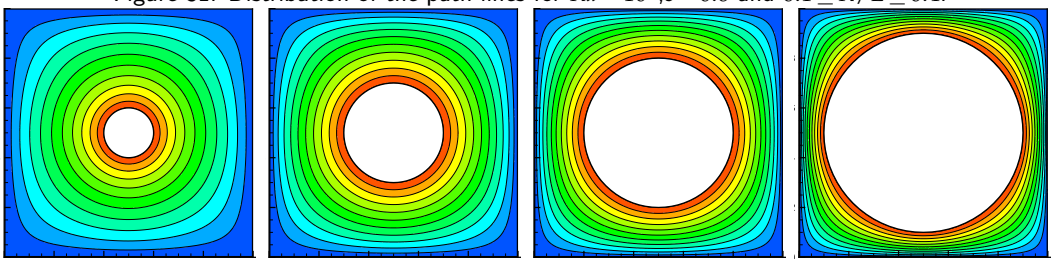

Figure 32: Distribution of the path lines for $Ra = 10^4, \varepsilon = 0.005$ and $0.1 \leq R/L \leq 0.4$.

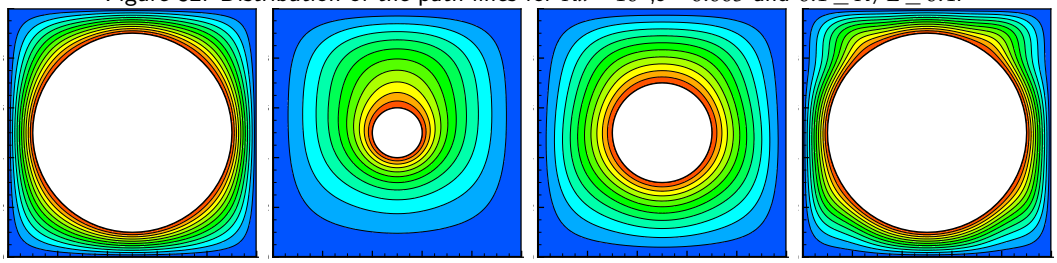

Figure 33: Distribution of the path lines for $Ra = 10^4, \varepsilon = 0.6$ and $0.1 \leq R/L \leq 0.4$.

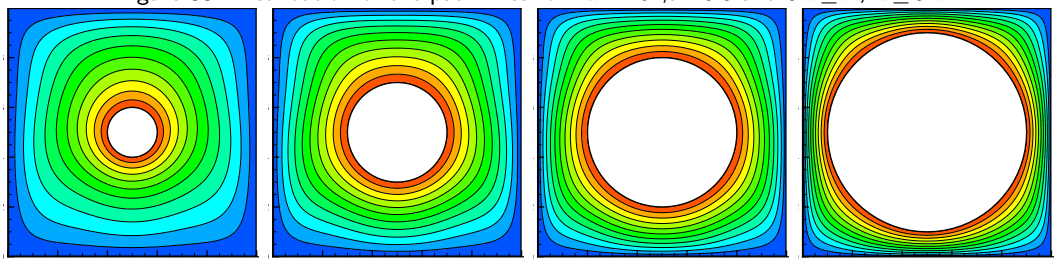

Figure 34: Distribution of the path lines for $Ra = 10^5, \varepsilon = 0.005$ and $0.1 \leq R/L \leq 0.4$.

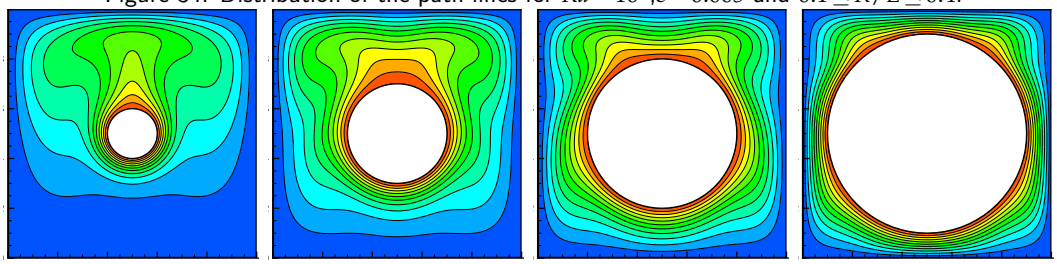

Figure 35: Distribution of the path lines for $Ra = 10^5, \varepsilon = 0.6$ and $0.1 \leq R/L \leq 0.4$.

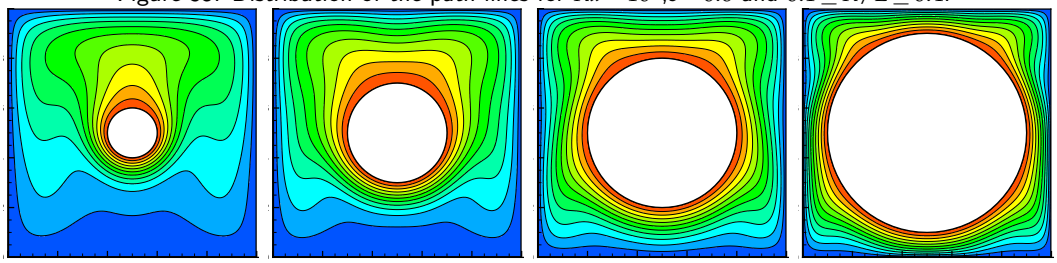

Figure 36: Distribution of the path lines for $Ra = 10^6, \varepsilon = 0.005$ and $0.1 \leq R/L \leq 0.4$.

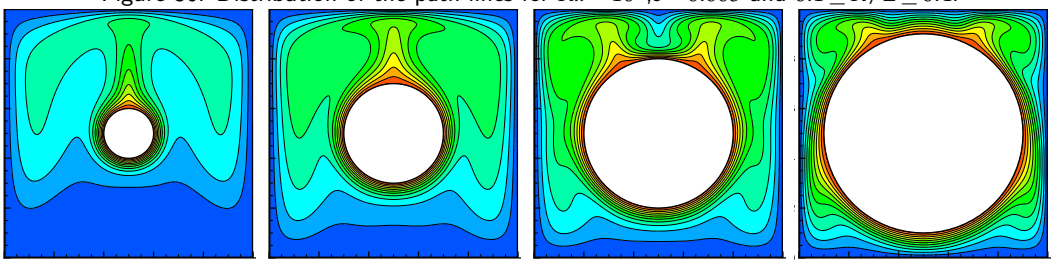

Figure 37: Distribution of the path lines for $Ra = 10^6, \varepsilon = 0.6$ and $0.1 \leq R/L \leq 0.4$.

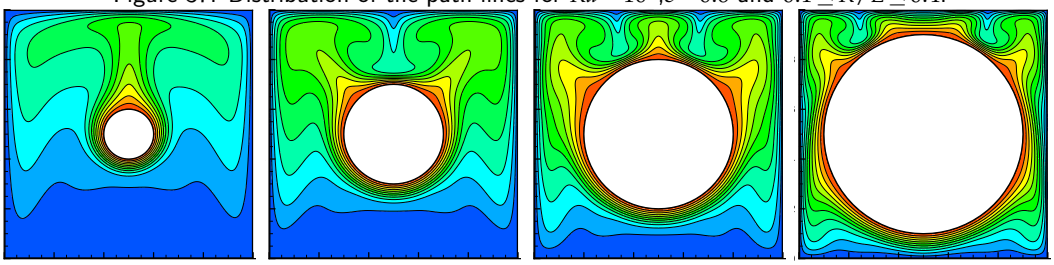

5.2 Quantitative results and discussion

5.2.1 Calculation of the Nusselt number

In this section, the discussion is focused on the average $\overline{Nu}_c$ and $\overline{Nu}_h$ values corresponding to the Nusselt numbers calculated at the cold cavity walls and at the cylinder surface, respectively. The calculation of $\overline{Nu}_c$ is based on the arithmetic average of the average Nusselt numbers at every wall of the cavity, each obtained by the method presented in subsection 4.2.2. The value of $\overline{Nu}_h$ is obtained by taking into account the heat flux from the cylinder's surface. Therefore, the average hot Nusselt number, $\overline{Nu}_h$ is:

$$\overline{Nu}_h = \frac{1}{2\varepsilon S} \int_S \rho C_p \frac{T_L^d - T_L}{\Delta t} dS. \tag{5.1}$$

The procedure of calculation of the $\overline{Nu}_h$ value does not require explicit calculation of the temperature gradients at the surface of the hot cylinder, rather it is an integral part of the IBM. Note that T_L is the temperature obtained at a specific Lagrangian point by interpolation of the corresponding predicted (i.e., obtained by not taking into account the existence of the immersed body) Eulerian temperature, which enables the calculation of $\overline{Nu}_h$ for both transient and steady-state flows.

5.2.2 Comparison of the results of the lowest-temperature-difference cases and previous studies

The results of the current study obtained for the value of $\varepsilon = 0.005$ were compared with those from corresponding studies of natural convection flow from a hot cylinder placed

Figure 38: Physical model of a hot cylinder inside a cold tube adapted from [28] and [43].

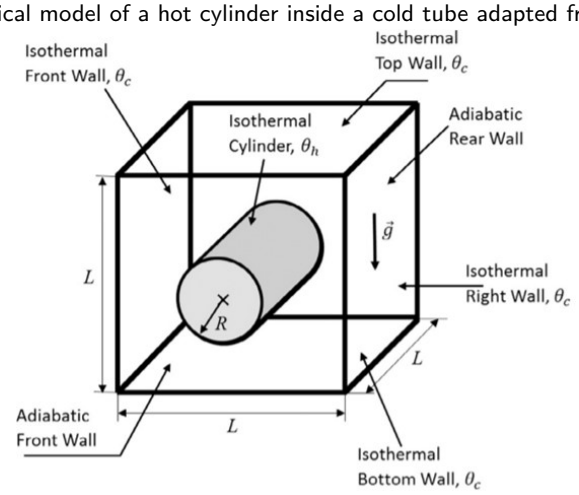

within a 3D cavity obtained by employing the Boussinesq approximation [28], [43] (see Fig. 38). Interestingly, there is acceptable agreement between our 2D study and the 3D results obtained in refs. [28], [43]in terms of $\overline{Nu}_h$ and $\overline{Nu}_c$ values for the whole range of Ra and R/L, as summarized in Tables 1-2. The maximal relative deviation between our results and the results obtained in refs. [28], [43] was 19% and could be attributed to the impact of the lateral walls in the 3D configuration suppressing the convective flow and thus decreasing the total heat flux.

5.2.3 Analysis of the heat fluxes in the flow domain

As mentioned in Section 2, , the walls of the cavity were maintained at a cold temperature $T_c = 1-\varepsilon$, while the walls of the cylinder that was placed in the center of the cavity were maintained at a hot temperature $T_h = 1+\varepsilon$. Therefore, the direction of the heat flux was from the cylinder surface toward the cavity surfaces. The value of heat flux at each cavity surface will reflect the characteristics of the specific flow regime and can thus be quantified by the calculation of the average values of $\overline{Nu}_c$ numbers for each wall. The $\overline{Nu}_c$ values were calculated by the formulas given in subsection 4.2.2.

As may be expected from symmetry considerations, the Nu values obtained for the left and right walls of the cavity were close to each other (see Tables 3-4) for the entire range of Ra-R/L values. At the same time, there were significant differences in the $\overline{Nu}_c$ values obtained for the bottom and top walls of the cavity (see Tables 5-6) for the entire range of Ra-R/L values, with the Nu values at the top always being higher than those at the bottom. These differences increased with increasing Ra values, and for $Ra = 10^6$ could reach up to one order of magnitude. To summarize, as the convective heat transfer became more pronounced with increasing Ra values, the top of the cavity started to play a more dominant role in removing heat from the system, which was clearly reflected in a gradual increase in the corresponding Nu values.

Table 1: Comparison between the present and the previously published $\overline{Nu}_h$ values averaged over the surface of a hot cylinder placed within a cold cube for $\varepsilon = 0.005$.

	Non-Boussinesq	Boussinesq		Non-Boussinesq	Boussinesq	
R/L	0.1			0.2		
Ra	Present	Ref. [28]	Ref. [43]	Present	Ref. [28]	Ref. [43]
10^4	6.4920	6.4880	6.2493	5.1990	5.1500	5.1184
10^5	11.8700	11.6620	11.1380	7.7780	7.5800	7.2271
10^6	18.1000	19.2500	18.3260	14.3500	13.3610	13.9370
R/L	0.3			0.4		
Ra	Present	Ref. [28]	Ref. [43]	Present	Ref. [28]	Ref. [43]
10^4	6.2630	5.7304	5.8084	8.8840	8.5544	8.7030
10^5	7.3740	6.5169	6.4790	9.1240	8.7643	8.7030
10^6	13.3600	11.4010	11.2720	11.9200	10.8320	10.7160

Table 2: Comparison between the present and the previously published $\overline{Nu}_c$ values averaged over the surface of a hot cylinder placed within a cold cube for $\varepsilon = 0.005$.

	Non-Boussinesq	Boussinesq		Non-Boussinesq	Boussinesq	
R/L	0.1			0.2		
Ra	Present	Ref. [28]	Ref. [43]	Present	Ref. [28]	Ref. [43]
10^4	1.0345	1.0208	1.0201	1.6662	1.6188	1.6161
10^5	1.9112	1.8360	1.8099	2.5649	2.3814	2.3766
10^6	2.8683	3.0348	2.9945	4.6134	4.3677	4.3985
R/L	0.3			0.4		
Ra	Present	Ref. [28]	Ref. [43]	Present	Ref. [28]	Ref. [43]
10^4	2.8655	2.9091	2.6216	5.4591	5.3928	5.1919
10^5	3.3675	3.0702	2.9726	5.6192	5.5131	5.2651
10^6	6.1671	5.3844	5.1956	7.2361	6.8313	6.6106

Table 3: Nu_c on the left wall.

ε	0.005				0.2			
R/L	0.1	0.2	0.3	0.4	0.1	0.2	0.3	0.4
Ra								
10^3	0.9389	1.5939	2.8186	5.4620	0.9877	1.5958	2.7040	5.4354
10^4	0.9287	1.6347	2.8549	5.4550	1.0373	1.6550	2.7334	5.4341
10^5	1.4945	2.3019	3.1750	5.5250	1.7238	2.2965	3.0942	5.5877
10^6	2.2876	4.5233	6.0957	7.5126	2.3220	3.7539	5.3523	7.3707
ε	0.4				0.6			
R/L	0.1	0.2	0.3	0.4	0.1	0.2	0.3	0.4
Ra								
10^3	0.9671	1.5791	2.6765	5.3313	0.9276	1.5618	2.6305	5.1832
10^4	1.0173	1.6197	2.6896	5.3356	0.9774	1.5729	2.6453	5.1905
10^5	1.7228	2.3632	3.1533	5.5551	1.7032	2.3394	3.1851	5.4981
10^6	2.3817	3.7652	6.3741	7.0895	2.3033	4.6269	6.1530	7.9808

Table 4: Nu_c on the right wall.

ε	0.005				0.2			
R/L	0.1	0.2	0.3	0.4	0.1	0.2	0.3	0.4
Ra								
10^3	0.9392	1.5945	2.8197	5.4640	0.9840	1.5976	2.7048	5.4374
10^4	0.9291	1.6354	2.8559	5.4570	1.0337	1.6583	2.7340	5.4361
10^5	1.4950	2.3030	3.1760	5.5270	1.7275	2.2982	3.0925	5.5897
10^6	2.8784	4.5249	6.0970	7.5153	2.3751	3.6198	5.5117	7.3734
ε	0.4				0.6			
R/L	0.1	0.2	0.3	0.4	0.1	0.2	0.3	0.4
Ra								
10^3	0.9612	1.5818	2.6775	5.3333	0.9235	1.5625	2.6315	5.1851
10^4	1.0119	1.6241	2.6905	5.3375	0.9750	1.0880	2.2705	5.1924
10^5	1.7259	2.3645	3.1544	5.5571	1.7048	2.3403	3.1862	5.5001
10^6	2.4127	3.8251	6.3767	7.0920	2.2621	4.6286	6.1556	7.9837

Table 5: Nu_c on the bottom wall.

ε	0.005				0.2			
R/L	0.1	0.2	0.3	0.4	0.1	0.2	0.3	0.4
Ra								
10^3	0.8819	1.5548	2.7986	5.4534	0.9575	1.5546	2.6772	5.4229
10^4	0.5861	1.3616	2.6723	5.3717	0.8554	1.3812	2.4982	5.3157
10^5	0.2150	0.7787	1.9192	4.8322	0.2756	0.6655	1.7119	4.6725
10^6	0.2358	0.7924	1.3864	7.5153	0.2299	0.3993	0.7655	3.1495
ε	0.4				0.6			
R/L	0.1	0.2	0.3	0.4	0.1	0.2	0.3	0.4
Ra								
10^3	0.9308	1.5322	2.6421	5.3133	0.8861	1.4995	2.5864	5.1582
10^4	0.8119	1.2999	2.3834	5.1648	0.7617	1.0880	2.2705	4.9589
10^5	0.2707	0.6223	1.2821	4.2901	0.2845	0.3204	1.1078	3.9579
10^6	0.2032	0.4767	0.6584	2.6102	0.1486	0.1582	0.4593	2.0442

Table 6: Nu_c on the top wall.

ε	0.005				0.2			
R/L	0.1	0.2	0.3	0.4	0.1	0.2	0.3	0.4
Ra								
10^3	1.0040	1.6374	2.8412	5.4732	1.0177	1.6432	2.7330	5.4502
10^4	1.6941	2.0329	3.0787	5.5527	1.2933	2.0418	3.0288	5.5709
10^5	4.4403	1.8762	5.1999	6.5926	4.2639	4.9223	5.3219	6.9002
10^6	5.4828	8.6132	11.0893	10.2210	7.2042	9.7895	9.3328	11.2149
ε	0.4				0.6			
R/L	0.1	0.2	0.3	0.4	0.1	0.2	0.3	0.4
Ra								
10^3	1.0012	1.6333	2.7134	5.3519	0.9687	1.6273	2.6768	5.2105
10^4	1.3028	2.0593	3.0640	5.5315	1.2711	2.1806	3.0940	5.4540
10^5	3.8549	4.5273	5.0862	7.0268	3.3704	3.9956	4.8861	6.9461
10^6	6.9131	9.2124	10.5519	10.8403	6.3005	7.8221	9.9085	10.7687

5.2.4 Approximation to the Nu-Ra power law

The results of the average Nusselt number for each configuration can be approximated, by employing the least squares technique, to obtain the $Nu-Ra$ power law. Following the dimensional analysis stemming from the boundary layer theory, the $Nu-Ra$ relationship obeys the following power law [44]:

$$\overline{Nu}_f = C(Gr \cdot Pr)^m = C(Ra)^m, \tag{5.2}$$

where Gr, Pr are the Grashof and Prandtl numbers and $Ra=GrPr$, and C and m are specific constants, whose values depend on the Ra number and on the geometric properties of the system under consideration.

Figures 39-42 present the distribution of the Nu number as a function of the Ra number for the entire range of: $\varepsilon \in \{0.005, 0.2, 0.4, 0.6\}$, $Ra \in \{10^4, 10^5, 10^6\}$ and $R/L \in \{0.1, 0.2, 0.3, 0.4\}$. Note that the Nu values obtained for the lowest value of $Ra = 10^3$ were not taken into account because of the dominance of the conductive heat transfer mechanism (see also Figs. 22-23 and Figs. 30-31).

All Nu values were approximated to the Nu-Ra power law as formulated by Eq. (5.2). Generally, acceptable accuracy was obtained when approximating the $Nu-Ra$ relationship by the power law for the entire range of ε and R/L values. The results obtained for smaller cylinders (R/L=0.1,0.2) exhibited more precise power law fits, for which the smallest value of R^2 was equal to $R^2 = 0.975$. Remarkably, for all configurations characterized by these R/L values, Nu was approximately proportional to $Ra^{0.22}$, which is very close to the results reported with respect to laminar natural convection in spherical shells [45–47].

Configurations with larger cylinders (R/L=0.3,0.4) exhibited slightly less pronounced power law fits for the $Nu-Ra$ relationship characterized by smallest value of R^2, i.e., $R^2 = 0.84$. Note also that Nu was approximately proportional to $Ra^{0.16}$ and to $Ra^{0.06}$ for the $R/L = 0.3$ and $R/L = 0.4$ geometries, respectively. Such a considerable decrease in the heat flux rate for geometries characterized by large cylinders compared to these characterized by smaller cylinders can be attributed to the blocking effects of both the cylinder and the cavity boundaries, which suppress the momentum of the convective flow (see e.g. [28], [43]).

5.2.5 Multiple steady-state regimes

Further numerical analysis revealed that steady non-Boussinesq natural convection flows can exhibit multiple steady-state regimes. In particular, two independent steady-state branches were found for the values of $\varepsilon = 0.4$, $R/L = \{0.2, 0.4\}$ and $Ra = 10^6$ as shown in Figs. 43-46 The stability of the revealed regimes was verified by randomly perturbing all the flow variables with values deviating by about 10% from the corresponding steady-state values and verifying that the flow then converged to the previously observed steady state. Remarkably, while the corresponding steady states differed in terms of the number and the size of the convective cells hosted within the flow domain, they were characterized by very close Nu values, averaged over the cylinder and the cavity boundaries. It can

Figure 39: Nusselt vs. Rayleigh numbers for $R/L = 0.1$.

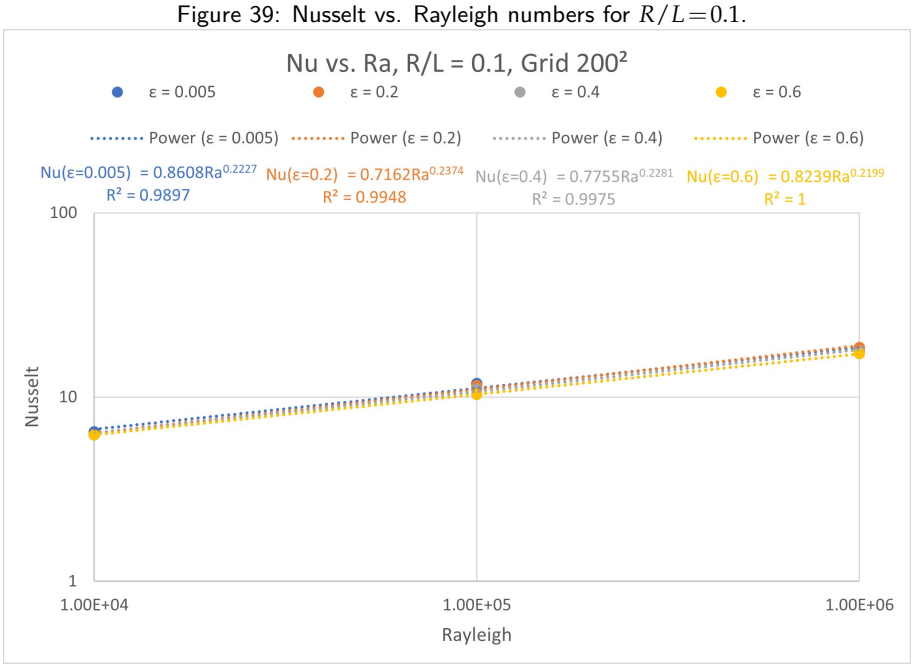

Figure 40: Nusselt vs. Rayleigh numbers for $R/L = 0.2$.

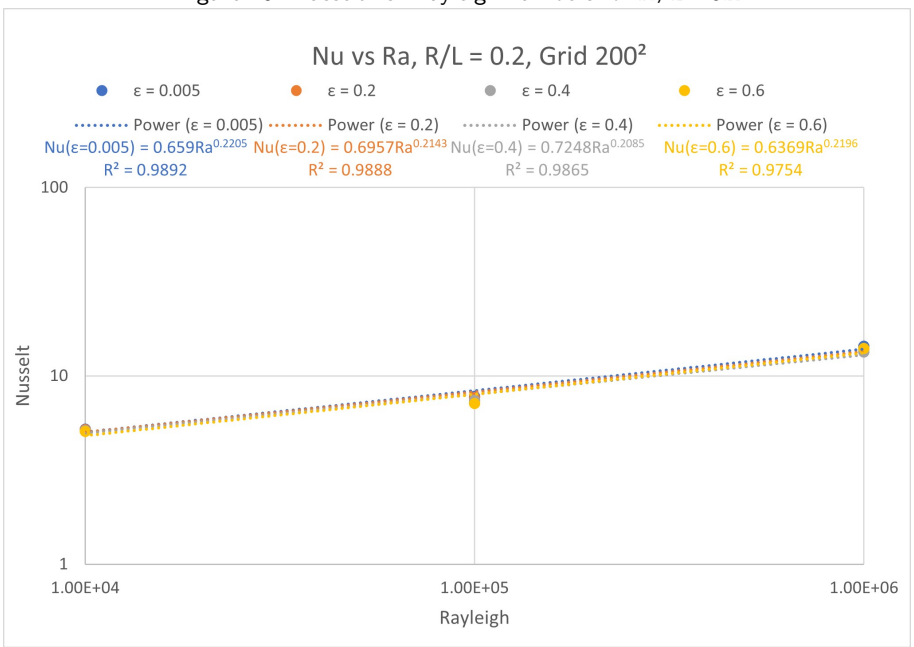

Figure 41: Nusselt vs. Rayleigh numbers for $R/L = 0.3$.

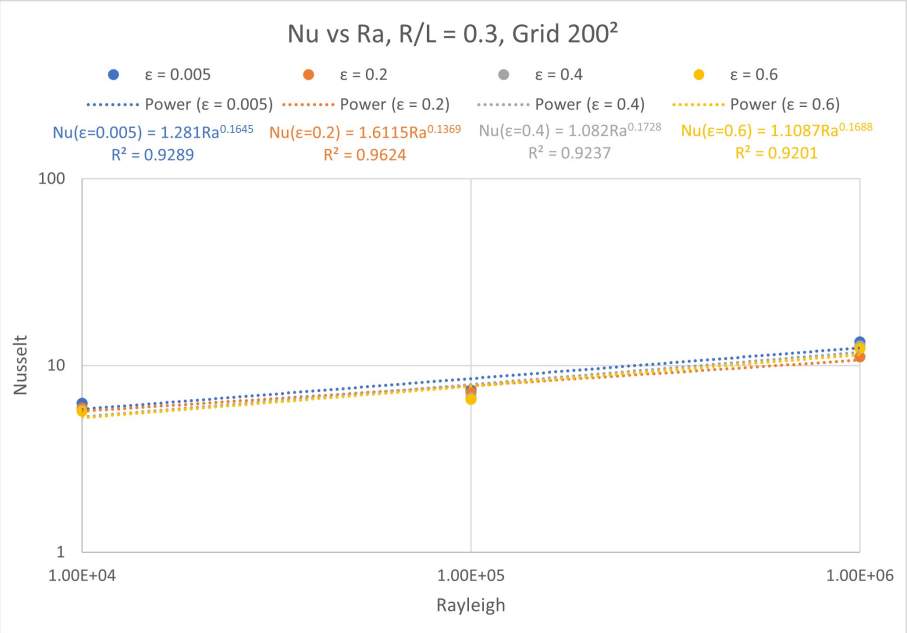

Figure 42: Nusselt vs. Rayleigh numbers for $R/L = 0.4$.

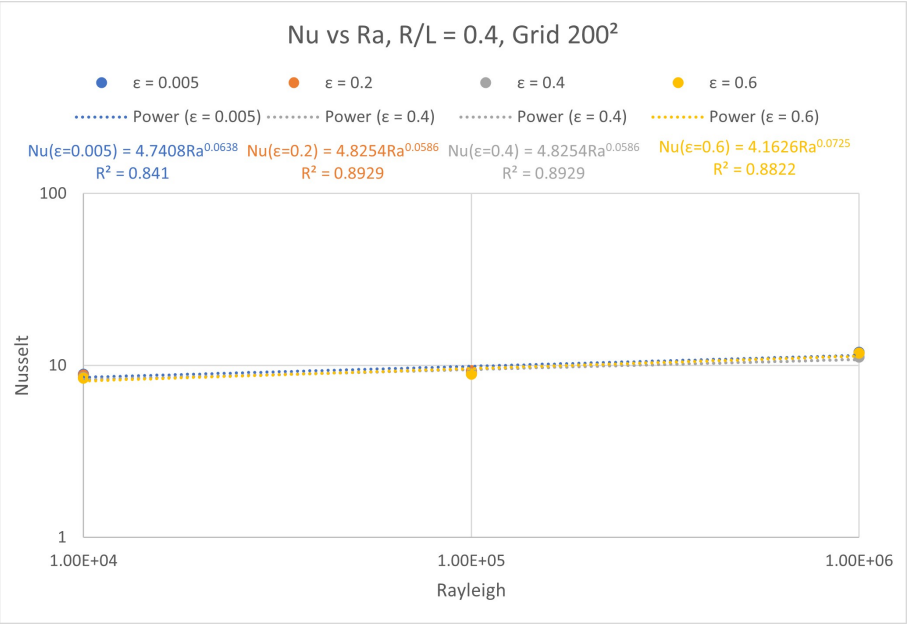

Figure 43: Flow and temperature patterns corresponding to two different steady state branches obtained for $\varepsilon = 0.4$, $Ra = 10^6$ and $R/L = 0.2$.

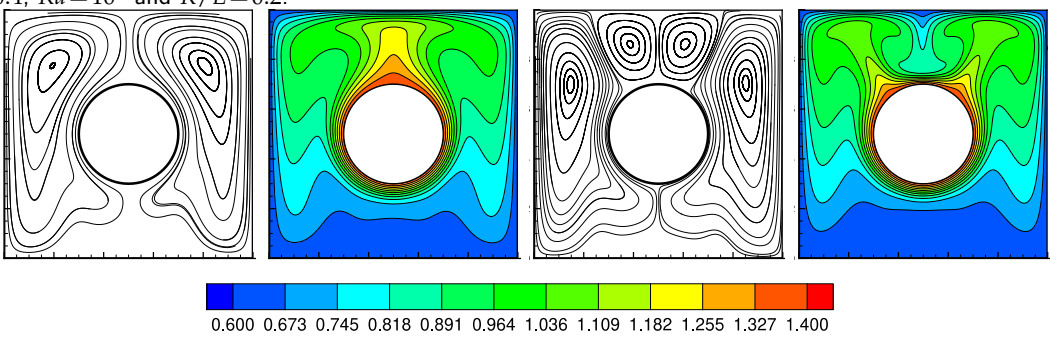

Figure 44: Flow and temperature patterns corresponding to two different steady state branches obtained for $\varepsilon = 0.4$, $Ra = 10^6$ and $R/L = 0.3$.

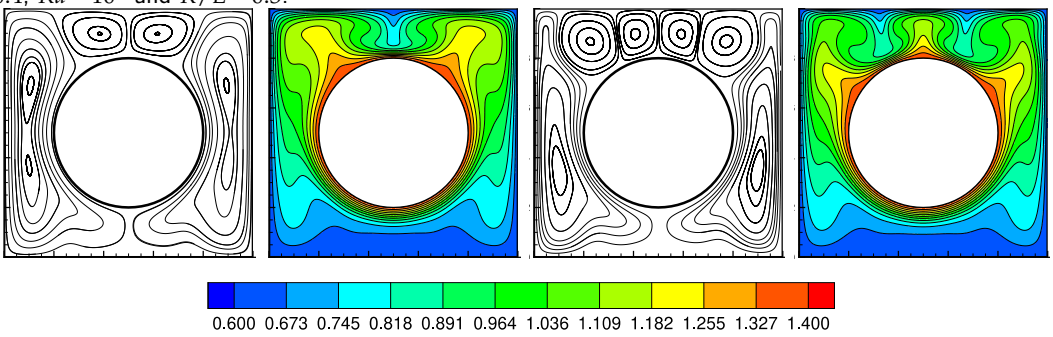

thus be concluded that both steady-state regimes obtained for the same values of the governing parameters and belonging to the different branches were still characterized by the same averaged heat fluxes at all the flow boundaries. In summary, acceptable agreement was obtained between our results for the lowest temperature-difference cases and results in the literature that were computed by applying the Boussinesq approximation for the entire range of operating conditions and flow characteristics; this agreement verifies the suitability of our numerical methodology with an incorporated IBM for simulation of compressible natural convection confined flows with complex geometry. The results of the high-temperature-gradient cases showed good agreement with the boundary layer theory. In addition, multiple configurations of the steady-state flow were discovered.

6 Conclusions

In the present work, a pressure-based solver for the simulation of the thermal compressible natural convection non-Boussinesq flow of an ideal gas was developed. This solver utilizes a second-order backward scheme and standard second-order finite volume method for temporal and spatial discretizations, respectively. The novel pressure-corrected direct

Figure 45: Flow and temperature patterns corresponding to two different steady state branches obtained for $\varepsilon = 0.4$, $Ra = 10^6$ and $R/L = 0.4$.

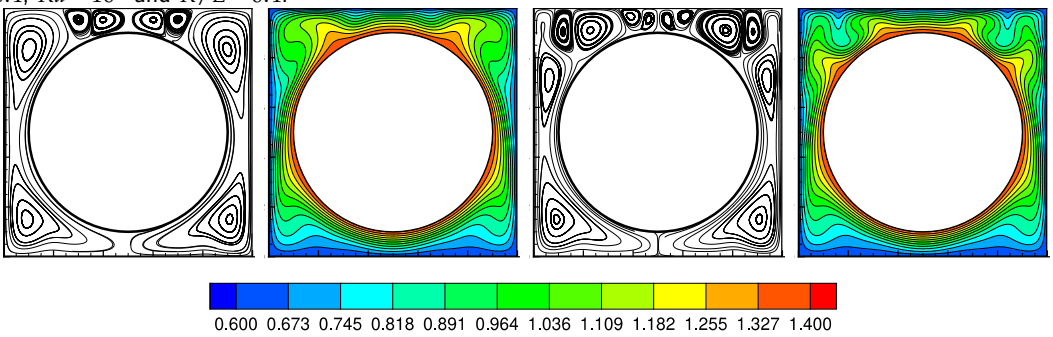

Figure 46: Flow and temperature patterns corresponding to two different steady state branches obtained for $\varepsilon = 0.6$, $Ra = 10^6$ and $R/L = 0.2$.

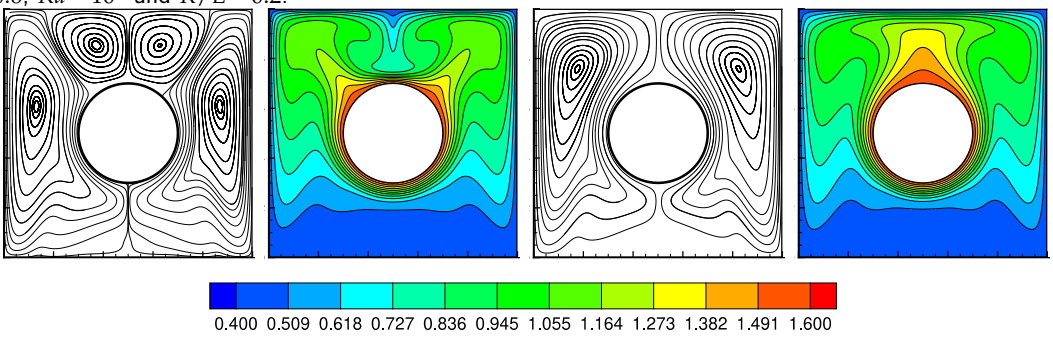

forcing IBM developed by Riahi et al. [33] was adopted and extended to enforce the kinematic constraints of no-slip and of a given temperature on the surface of the immersed body. The algorithm does not rely on the low-Mach-number assumption and does not employ the methodology of splitting the pressure into hydrodynamic and thermodynamic terms. Instead, all the equations are solved in their original fully compressible formulations. Finally, the viscous heating is neglected, as is commonly done when simulating flows characterized by low values of the shear stress.

The developed methodology was extensively verified by comparison with corresponding independently obtained numerical data available in the literature for incompressible flows [42] and non-Boussinesq compressible flows [4]. The pressure-corrected direct forcing IBM was implemented for simulation of the natural convection non-Boussinesq flow developing within a cold square cavity with a centrally located hot cylinder over a broad range of governing parameters. The results obtained were analyzed qualitatively and quantitatively. First, the spatial distributions of the path lines and temperature fields were obtained. Second, the values of Nusselt number on the hot cylinder and the cold cavity surfaces were calculated. Third, the thermal fluxes at all the domain boundaries were quantified by calculating the values of the corresponding Nusselt numbers. Finally, multiple steady-state solutions for several configurations were discovered.

Two different strategies, one based on an iterative solution and the other, on a direct solution of the discretized governing equations were applied in the current study. The iterative solution utilized the BiCGstab method [38], while the direct solution was based on the TPF method proposed by Lynch et al. [39] and subsequently adapted to confined natural convection flows by Vitoshkin & Gelfgat in [40]. The major challenge in applying the two methods lay in treating the non-linear terms and the temperature-dependent coefficients of the Helmholtz-like differential operator, which were obviously not constant. It was found that in the absence of an immersed body both the iterative solver and the direct solver yielded sufficiently accurate solutions for non-Boussinesq flows. However, in the presence of an immersed body, the iterative solver based on the BiCGstab method was less sensitive to the time step values and provided more accurate results than its direct counterpart based on the TPF method.

We summarize by giving a list of challenges that have been left out the scope of the current study and need to be addressed further on the way of developing a systematic pressure-based numerical framework for simulating non-Boussinesq natural convection flows. The first challenge is the development of the method for simulating the flow around moving bodies. In this case, it is well known that the direct forcing method can lead to spurious non-physical oscillations if explicitly included in the fractional step approach (see e.g. [34]). The problem can be remedied by utilizing semi-implicit formulation of the immersed boundary method, which imposes kinematic constraints of no-slip on the predicted non-solenoidal velocity field up to machine zero precession [48]. The second challenge is an extension of the currently presented method to simulate fully 3D natural convection flows. Based on our previous work, which utilized an explicit implementation of the direct forcing method to simulate steady state Boussinesq natural convection flows [49] we do not

Figure 47: Relative spatial error of the developed algorithm calculated for the values of $\varepsilon = 0.6$ and $Ra = 10^6$ for the θ (•),u (♦), and v (▲) fields: (a) l_2 norm; (b) l_∞ norm.

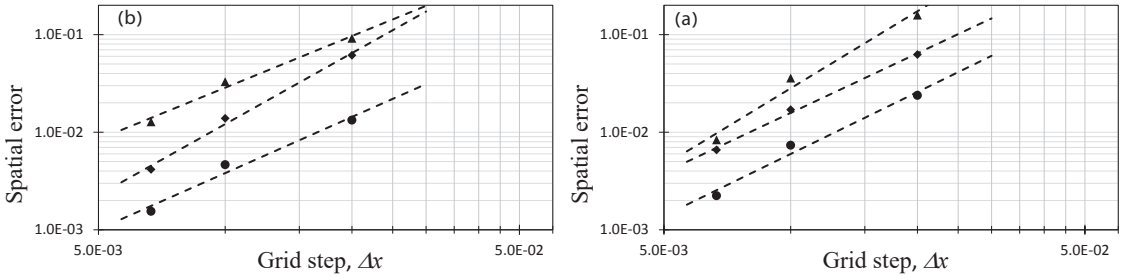

see any objective reasons that could prevent the direct adaption of the currently presented method for simulation of non-Boussinessq natural convection steady 3D flows. Again, in the case of the appearance of spurious oscillations in the flow fields when simulating unsteady natural convection flows, it may be necessary to switch from a completely explicit implementation of the direct forcing to its semi-implicit counterpart (see e.g. [28]). Finally, the developed method needs further verification to simulate the flow around bodies characterized by non-uniform curvature. In this case, the grid resolution must be adjusted to a kernel of the selected discrete Dirac delta function to ensure that the results provided by the interpolation and regularization operators acting on the flow fields are sufficiently accurate.

7 Acknowledgements

The authors would like to thank the Israel Ministry of Energy for its financial support for this work (grant 218-11-038).

A Appendix: Estimation of the method accuracy

To further evaluate the accuracy of the steady-state solutions obtained in this study, we present a formal analysis of the spatial accuracy of the results obtained. The analysis has been performed by calculating the values of Euclidian and infinity norms of relative errors $\|S_{ex} - S_{apr}\| / \|S_{ex}\|$, where S_{ex} corresponds to the most precise solution obtained on 200×200 grid and S_{apr} corresponds to a series of approximate solutions obtained on 50×50, 100×100 and 1500×150 grids. The data calculated for temperature and two velocity components obtained for the steady state flow in a deferentially heated cavity for the values of $\varepsilon = 0.6$ and $Ra = 10^6$ is presented in Fig. 47. It can be seen that there is a power-law relationship between Δx and the norm of the relative error value. In all presented cases, the value of the exponent is close to 2, which confirms the second order spatial accuracy of the developed method.

References

[1] P. Mayeli and G. J. Sheard, "Buoyancy-driven flows beyond the Boussinesq approximation: A brief review," International Communications in Heat and Mass Transfer, vol. 125, 2021.

[2] R. G. Rehm and H. R. Baum, "The Equations of Motion for Thermally Driven, Buoyant Flows," Jouranl of Research of the National Bureau of Standards, vol. 83, no. 3, 1978.

[3] S. Paolucci, "On the Filtering of Sound from the Navier-Stokes Equations," Analytical Thermal/Fluid Mechanics Division, Sandia National Laboratories, Livermore, 1982.

[4] D. R. Chenoweth and S. Paolucci, "Natural Convection in enclosed vertical air layer with large horizontal temperature differences," Journal of Fluid Dynamics, vol. 169, pp. 173-210, 1986.

[5] S. Paolucci, "The differentially heated cavity," Sadhana, vol. 19, no. 5, pp. 619-647, 1994.

[6] P. Le Querre, R. Masson and P. Perrot, "A Chebyshev Collocation Algorithm for 2D Non-Boussinesq Convection," Journal of Computational Physics, vol. 103, pp. 320-335, 1992.

[7] H. Paillere, C. Viozat, A. Kumbaro and I. Toumi, "Comparison of low Mach number models for natural convection problems," Heat and Mass Transfer, vol. 36, no. 6, pp. 567-573, 2000.

[8] M. Elmo and O. Cioni, "Low Mach number model for compressible flows and application to HTR," Nuclear Engineering and Design, vol. 222, no. 2-3, pp. 117-124, 2003.

[9] E. Schall, C. Viozat, B. Koobus and A. Dervieux, "Computation of low Mach thermical flows with implicit upwind methods," International Heat and Mass Transfer, vol. 46, no. 20, pp. 3909-3926, 2003.

[10] O. Le Maitre, M. T. Reagan, B. Debusschere, H. N. Nahm, R. G. Ghanem and O. M. Knio, "Natural Convection in a Closed Cavity Under Stochastic Non-Boussinessq Conditions," SIAM Journal on Scientific Computing, vol. 26, no. 2, pp. 375-394, 2004.

[11] A. Beccantini, E. Studer, S. Gounand, J. P. Magnaud, T. Kloczko, C. Corre and S. Kudriakov, "Numerical simulations of a transient injection flow at low Mach number regime," International Journal for Numerical Methods in Engineering, vol. 76, no. 5, pp. 662-696, 2008.

[12] P. V. Reddy, G. V. Narashinbam, S. R. Rao, T. Johny and K. V. Kasiviswanathan, "Non-Boussinesq conjugate natural convection in a vertical annulus," International Communications in Heat and Mass Transfer, vol. 37, no. 9, pp. 1230-1237, 2010.

[13] M. Lappa, "A mathematical and numerical framework for the analysis of compressible thermal convection in gases at very high temperatures," Journal of Computational Physics, vol. 313, pp. 687-712, 2016.

[14] J. M. Armengol, F. C. Bannwart, J. Xaman and R. G. Santos, "Effects of variable air properties on transient natural convection for large temperature differences," International Journal of Thermal Sciences, vol. 120, pp. 63-79, 2017.

[15] W.-S. Fu, C.-G. Li, C.-P. Huang and J.-C. Huang, "An investigation of a high temperature difference natural convection in a finite length channel without Bossinesq assumption," International Journal of Heat and Mass Transfer, vol. 52, no. 11-12, pp. 2571-2580, 2009.

[16] M. M. El-Gendi and A. Aly, "Numerical simulation of natural convection using unsteady compressible Navier-stokes equations," International Journal of Numerical Methods for Heat & Fluid Flow, vol. 27, no. 11, pp. 2508-2527, 2017.

[17] C.-G. Li, "A compressible solver for the laminar-turbulent transition in natural convection with high temperature differences using implicit large eddy simulation," International Communications in Heat and Mass Transfer, vol. 117, 2020.

[18] J. H. Ferziger, M. Perić and R. L. Street, Computational Methods for Fluid Dynamics. Fourth Edition, Stanford, CA, USA: Springer Nature Switzerland AG, 2020.

[19] F. Moukalled and M. Darwish, "A Unified Formulation of the Segregated Class of Algorithms for Fluid Flow at All Speeds," Numerical Heat Transfer Part B - Fundamentals, vol. 37, no. 1, pp. 103-139, 2000.

[20] E. A. Sewall and D. K. Tafti, "A time-accurate variable property algorithm for calculating flows with large temperature variations," Computers & Fluids, vol. 37, no. 1, pp. 51-63, 2008.

[21] H. Barrios-Pina, S. Viazzo and C. Rey, "Total energy balance in a natural convection flow," International Journal of Numerical Methods for Heat & Fluid Flow, vol. 27, pp. 1735-1747, 2017.

[22] C. S. Peskin, "The immersed boundary method," Acta Numerica , vol. 11, pp. 479-517, 2002.

[23] M. H. Sedaghat, A. A. Bagheri, M. M. Shahmardan, M. Norouzi, B. C. Khoo and P. G. Jayathilake, "A Hybrid Immersed Boundary-Lattice Bolyzmann Method for Simulation of Viscoelastic Fluid Flows Interaction with Complex Boundaries," Commun. Comput. Phys., vol. 29, pp. 1411-1445, 2021.

[24] B. S. Kim, D. S. Lee, M. Y. Ha and H. S. Yoon, "A numerical study of natural convection in a square enclosure with a circular cylinder at different vertical locations," International Jouranl of Heat and Mass Transfer, vol. 51, pp. 1888-1906, 2008.

[25] C. C. Liao and C. A. Lin, "Influences of a confined elliptic cylinder at different aspect ratios and inclinations on the laminar natural and mixed convection flows," International Journal of Heat and Mass Transfer, vol. 55, pp. 6638-6650, 2012a.

[26] H. K. Park, M. Y. Ha, H. S. Yoon, Y. G. PArk and C. Son, "A numerical study on natural convection in an inclined square enclosure with a circular cylinder," International Journal of Heat and Mass Transfer, vol. 66, pp. 295-314, 2013a.

[27] Y. G. Park, M. Y. Ha and H. S. Yoon, "Study on natural convection in a cold sphere enclosure with a pair of hot horizontal cylinders positioned at different vertical locations," International Jpournal of Heat and Mass Transfer, vol. 65, pp. 696-712, 2013b.

[28] Y. Feldman, "Semi-implicit direct forcing immersed boundary method for incompressible viscous thermal flow problems: A Schur complement approach," International Journal of Heat and Mass Transfer, vol. 127, pp. 1267-1283, 2018.

[29] S. H. Lee, Y. M. Seo, H. S. Yoon and M. Y. Ha, "Three-dimensional natural convection around an inner circular cylinder located in a cubic enclosure with sinusoidal thermal boundary condition," International Journal of Heat and Mass Transfer, vol. 101, pp. 807-823, 2016.

[30] Y. M. Seo, J. H. Doo and M. Y. Ha, "Three-dimensional flow instability of natural convection induced by variation in radius of inner circular cylinder inside cubic enclosure," International Journal of Heat and Mass Transfer, vol. 95, pp. 566-578, 2016.

[31] A. Spizzichino, E. Zemach and Y. Feldman, "Oscillatory instability of a 3D natural convection flow around a tandem of cold and hot vertically aligned cylinders placed inside a cold cubic enclosure," International Journal of Heat and Mass Transfer, vol. 141, pp. 327-345, 2019b.

[32] E. Zemach, A. Spizzichino and Y. Feldman, "Instability characteristics of a highly separated natural convection flow: Configuration of a tandem of cold and hot horizontally oriented cylinders placed within a cold cubic enclosure," International Journal of Heat and Mass Transfer, p. 106606, 2021.

[33] H. Riahi, M. Meldi, J. Favier, E. Serre and E. Goncalves, "A pressure-corrected Immersed Boundary Method for the numerical simulation of compressible flows," Journal of Computational Physics, vol. 374, pp. 361-383, 2018.

[34] M. Kumar and G. Natarajan, "Diffuse interface immersed boundary method for low Mach number flows with heat transfer in enclosures," Physics of Fluids, vol. 31, 2019.

[35] S. V. Patankar, Numerical Heat Transfer and Fluid Flow, New York: Hemisphere, 1981.

[36] A. M. Roma, C. S. Peskin and M. J. Berger, "An Adaptive Version of the ImmersedBoundary Method," Journal of Computational Physics, vol. 153, pp. 509-534, 1999.
[37] K. Taira and T. Colonius, "The immersed boundary method: A projection approach," Journak of Computational Physics, vol. 225, pp. 2118-2137, 2007.
[38] W. H. Press, S. A. Teukolsky, W. T. Vetterling and B. P. Flannery, Numerical Recipes in Fortran 77: The Art of Scientific Computing, Cambridge: Cambridge University Press, 1989.
[39] R. E. Lynch, J. R. Rice and D. H. Thomas, "Direct solution of partial differential equations by tensor product methods," Numerical mathematics, vol. 6, pp. 185-199, 1964.
[40] H. Vitoshkin and A. Y. Gelfgat, "On direct inverse of Stokes, Helmholtz and Laplacian operators in view of time-stepper-based Newton and Arnoldi solvers in incompressible CFD," Communications in Computational Physics, vol. 14, pp. 1103-1119, 2013.
[41] A. Y. Gelfgat, "On acceleration of Krylov-subspace-based Newton and Arnoldi iterations for incompressible CFD: replacing time steppers and generation of initial guess," in Computational modelling of Bifurcations and Instabilities in Fluid Dynamics, Berlin/Heidelberg, Germany, Springer, 2018, pp. 147-167.
[42] D. K. Gartling, "A Test Problem for Outflow Boundary Conditions - Flow over a Backward Facing Step," International Journal for Numerical Methods in Fluids, vol. 11, no. 7, pp. 953-967, 1990.
[43] Y. M. Seo, J. H. Doo and M. Y. Ha, "Three-dimensional Flow Instability of Natural Convection Induced by Variation in Radius of Inner Circular Cylinder Inside Cubic Enclosure," International Journal of Heat and Mass Transfer , vol. 64, pp. 514-525, 2013.
[44] J. P. Holman, "Chapter 7. Natural Convection Systems," in Heat Transfer, Tenth Edition, Avenue of the Americas, New York, NY 10020, McGraw-Hill, a business unit of The McGraw-Hill Companies, Inc., 1221, 2010, pp. 327-378.
[45] J. A. Scanlan, E. H. Bishop and R. E. PoweR., "Natural Convection Heat Transfer Between Concentric Spheres," International Journal of Heat and Mass Transfer, vol. 13, pp. 1857-1872, 1970.
[46] G. D. Raithby and K. G. Hollands, "A General Method of Obtaining Approximate Solutions to Laminar and Turbulent Free Convection Problems," Advances in Heat Transfer, vol. 11, pp. 265-315, 1975.
[47] P. Teertstra, M. M. Yovanovich and J. R. Culham, "Analytical Modelling of Natural Convection in Concentric Spherical Enclosures," Jouranl of Thermodynamics and Heat Transfer, vol. 20, pp. 297-304, 2006.
[48] R. Sela, E. A. Sela and Y. Feldman, "A Semi-Implicit Direct Forcing Immersed Boundary Method for Periodically Moving Immersed Bodies: A Schur Complement Approach," Comput. Methods Appl. Mech. Emgrg., vol. 373, pp. 113498, 2021.
[49] Y. Gulberg and Y. Feldman, "On Laminar Natural Convection Inside Multi-Layered Spherical Shells," Int. J. Heat Mass Transfer, vol. 91, pp. 908-921, 2015.